Microtubule stiffening by doublecortin-domain protein ZYG-8 contributes to spindle orientation during *C. elegans* zygote division

Authors:
Louis Cueff[1], Sylvain Pastezeur[1], Ewen Huet[1], Méline Coquil[1], Titouan Savary[1], Jacques Pécréaux[1,*], Hélène Bouvrais[1,*]

Affiliations:
[1] IGDR CNRS, Univ Rennes, IGDR (Institut de Génétique et Développement de Rennes) – UMR 6290, F-35000 Rennes, France
* Corresponding authors :
Jacques Pécréaux (ORCID : 0000-0001-9998-4844) and Hélène Bouvrais (ORCID : 0000-0003-1128-1322)
IGDR-UMR6290, CNRS-Université de Rennes
Faculté de Médecine
2 Av. du Professeur Léon Bernard,
CS 34317 - 35043 Rennes Cedex
France
Tel: +33 2 23 23 45 03 (JP), +33 2 23 23 40 08 (HB)
Email: jacques.pecreaux@univ-rennes.fr, helene.bouvrais@univ-rennes.fr

ABSTRACT

Microtubules are key players in cell division. Beyond their dynamic instability, we addressed the role(s) of microtubule flexural rigidity in spindle positioning. We used the nematode *Caenorhabditis elegans* zygote, which features a unique Doublecortin-family member ZYG-8^{DCLK1}, known to regulate microtubule rigidity in neurons. We showed that ZYG-8 regulates microtubule rigidity during the first division, as evidenced by more bent microtubules when *zyg-8* was targeted. Besides, they exhibited larger curvatures and increased tortuosity. Functionally, we observed increased amplitudes of anaphase spindle-pole oscillations following *zyg-8(RNAi)*. We demonstrated that this originated from the reduced cortical pushing-force due to softened microtubules. Oscillation amplitudes also increased when we depleted PTL-1^{Tau} that regulates microtubule rigidity. Interestingly, the *zyg-8(or484ts)* mutant, which prevents microtubule binding, exhibited even greater oscillations and incorrect final spindle position and orientation. Overly soft microtubules likely impair the spindle centring force, breaking the pulling versus pushing force balance. In conclusion, sufficient microtubule rigidity is essential during cell division to ensure effective microtubule cortical pushing, thereby accurately orienting the spindle. Beyond ensuring correct daughter cell fates in asymmetric divisions, we suggest that microtubule flexural rigidity is likely controlled in all mitoses, consistent with the reported deregulation of DCLK1 in various human solid tumours.

INTRODUCTION

Microtubules are semi-rigid polymers that form a crucial component of the cell cytoskeleton alongside actin and intermediate filaments. They perform essential functions with various molecular players, including cell shaping (Matis, 2020; Rizzelli et al., 2020), intracellular trafficking (Burute and Kapitein, 2019), and cell migration (Garcin and Straube, 2019). Microtubules play major roles in cell division; for example, spindle microtubules assemble into the mitotic spindle and segregate chromosomes, while astral microtubules help position the spindle (di Pietro et al., 2016; Forth and Kapoor, 2017; Kotak, 2019; Lechler and Mapelli, 2021; McNally, 2013; Thomas et al., 2017; van Leen et al., 2020). Each microtubule comprises protofilaments that are linear chains of tubulin dimers added or removed dynamically. Microtubule dynamic instability, characterised by stochastic transitions between growing and shrinking phases, is regulated *in vivo* by numerous Microtubule Associated Proteins (MAPs) (Akhmanova and Kapitein, 2022; Goodson and Jonasson, 2018; Gudimchuk and McIntosh, 2021). In contrast, the mechanical properties of microtubules, particularly their flexural rigidity—i.e., their resistance to bending—have received comparatively less attention. Notably, microtubules exhibit the highest flexural rigidity among cytoskeletal filaments (Gittes et al., 1993). While *in vitro* reconstituted microtubules are bent at the scale of a few millimetres (Felgner et al., 1996; Gittes et al., 1993; Kurachi et al., 1995; Mickey and Howard, 1995), *in vivo* observations revealed that microtubules appear bent at the micrometre scale (Brangwynne et al., 2006; Hawkins et al., 2010; Zhang et al., 2017). On the one hand, high microtubule rigidity is necessary for efficient intracellular trafficking (Balabanian et al., 2017) or pushing against obstacles, such as chromosome arms causing the polar ejection force (Maiato et al., 2017; Schneider et al., 2022). On the other hand, microtubules must also be flexible enough to bend and adapt to the shape of the cell as they navigate through the crowded cytoplasm (Arjona et al., 2023). It calls for regulating microtubule flexural rigidity *in vivo* to support various biological functions (Hawkins et al., 2010).

Several mechanisms have been proposed to achieve such a regulation, with two key families of proteins identified: the Doublecortin family, notably composed of DCX and DCLK1, and the MAP2/MAP4/Tau superfamily (Felgner et al., 1997; Kurachi et al., 1995; Mickey and Howard, 1995; Nishida et al., 2023). For instance, the simultaneous knockdown of DCX and DCLK1 in rat neurons led to more curved microtubules at the growing axon tip (Jean et al., 2012). Doublecortin family proteins associate with microtubules through their doublecortin domains. Notably, they bind between the microtubule protofilaments at the vertices of four tubulin dimers, contributing to the lateral coupling of adjacent protofilaments (Fourniol et al., 2010; Moores et al., 2004). This binding likely hinders protofilament sliding, making the microtubule stiffer (Pampaloni et al., 2006; Sui and Downing, 2010). Along a similar line, Tau-deficient axons have been shown to exhibit curled microtubules (Hahn et al., 2021). Tau family proteins bind longitudinally along the outer ridges of microtubule protofilaments. It would strengthen the longitudinal contacts between tubulin heterodimers within a protofilament, straightening them (Kadavath et al., 2015; Kellogg et al., 2018). Importantly, both protein families also contribute to the regulation of microtubule dynamics. *In vivo* studies indicate that these proteins stabilise microtubules and reduce their dynamics by decreasing catastrophe frequency, depolymerisation and nucleation rates, or promoting growth (Bunker et al., 2004; Dema et al., 2024; Hahn et al., 2021; Srayko et al., 2005). While the impacts of controlling microtubule rigidity have primarily been studied in neurons, microtubule-rigidity contribution during cell division also warrants investigations.

To explore this potential role, we reviewed previous cell-division studies targeting proteins from the Doublecortin and Tau families. Interestingly, targeting a protein from the Doublecortin family resulted in several cell division perturbations, including mispositioning of the mitotic spindle, defects in the formation and integrity of meiotic or mitotic spindles, and impaired mitotic progression (Couillard-Despres et al., 2004; Czajkowski et al., 2024; Gönczy et al., 2001; Kaplan and Reiner, 2011; Li et al., 2023; Shu et al., 2006; Vreugdenhil et al., 2007). During neurogenesis, some of these studies led to incorrect cell fate determination for neural progenitors (Shu et al., 2006; Vreugdenhil et al., 2007). Additionally, the deregulation of Tau (whether through mutation or overexpression) has been linked to mitotic defects, such as issues with spindle formation, aneuploidy and chromosome misalignment (Bougé and Parmentier, 2016; Rossi et al., 2008). Thus, targeting Doublecortin and Tau family proteins can lead to a wide range of meiotic and mitotic disturbances, though the underlying mechanisms remain unclear. Proposed explanations include perturbations in microtubule stability and molecular motor activity or recruitment (Czajkowski et al., 2024; Gönczy et al., 2001; Kaplan and Reiner, 2011; Li et al., 2023; Liu et al., 2012; Shu et al., 2006; Vreugdenhil et al., 2007). Whether the underlying mechanism of these mitotic or meiotic defects involves microtubule rigidity is yet to be thoroughly investigated in dedicated studies.

Along this line, we and others have proposed that microtubule buckling—i.e., bending under compressive forces—contributes to the precise and stable maintenance of the mitotic spindle at the cell centre during the metaphase of the *Caenorhabditis elegans* zygote division (Bouvrais et al., 2021; Garzon-Coral et al., 2016; Howard, 2006; Pécréaux et al., 2016). While, this division is asymmetric, the mitotic spindle initially orients along the polarity axis and centres within the embryo during prophase. It is then maintained at the cell centre during metaphase and is finally displaced toward the posterior side, mostly during anaphase (Oegema and Hyman, 2006). The correct positioning and orientation of the spindle during asymmetric divisions are critical for cell fate determination and, more broadly, for the organism's development (Lechler and Mapelli, 2021). These processes primarily depend on dynamic astral microtubules emanating from the centrosomes, which can transmit or generate three types of forces (Howard and Garzon-Coral, 2017; Kotak, 2019; McNally, 2013): first, cortical pulling forces mediated by dynein motors anchored at the cell cortex interacting with shrinking microtubules (Grill and Hyman, 2005; Kozlowski et al., 2007; Nguyen-Ngoc et al., 2007); second, cytoplasmic pulling forces involving motile dynein interacting with organelles within the cytoplasm (Kimura and Kimura, 2011); and third, cortical pushing forces generated by microtubules that grow against the cell cortex (Garzon-Coral et al., 2016; Howard, 2006; Pécréaux et al., 2016). Given that pushing forces rely on stiff microtubules, we proposed that their rigidity be controlled to ensure the proper choreography of the spindle during *C. elegans* division. Specifically, we envisioned that sufficiently high microtubule rigidity may be required to balance elevated cortical pulling forces during anaphase, the latter participating in spindle elongation and posterior displacement.

To address the potential role of microtubule flexural rigidity in cell division, we utilised the *C. elegans* embryo, a well-established model of asymmetric cell division with low functional redundancy. Notably, *zyg-8* and *ptl-1* are the only members of the Doublecortin and Tau families, respectively (Goedert et al., 1996; McDermott et al., 1996; Reiner et al., 2006). Mutations in doublecortin or kinase domains of *zyg-8* have been shown to induce incorrect spindle final positioning and orientation (Gönczy et al., 2001). Moreover, ZYG-8 depletion or mutation caused defective meiotic spindles, either longer and bent (still-bipolar) or multipolar

(Czajkowski et al., 2024; Li et al., 2023). Overall, it led us to target *zyg-8* to manipulate microtubule rigidity. We employed three complementary genetic perturbations: reducing ZYG-8 expression via RNA interference, overexpressing it and hindering its microtubule binding using a *zyg-8(or484ts)* mutant (Bellanger et al., 2007). We measured the distributions of microtubule local curvatures to assess variations in microtubule rigidity alongside examining spindle positioning through various biophysical techniques to get corresponding division phenotypes. Our findings demonstrate that ZYG-8 is needed to maintain the correct spindle orientation during mitosis, primarily by controlling the centring forces that depend on the microtubule flexural rigidity. Interestingly, the depletion of PTL-1 through RNAi exhibited a comparable but milder effect on spindle choreography compared to *zyg-8(RNAi)*. Our study highlights the need for sufficient microtubule rigidity for proper mitotic spindle positioning and orientation during *C. elegans* zygote division.

RESULTS

1- ZYG-8 likely regulates microtubule flexural rigidity.

As ZYG-8^{DCLK1} was suggested to control microtubule curvatures in neurons, we set out to validate its role in the one-cell embryo. We first investigated its localisation. By immunofluorescence, ZYG-8 was localised at the spindle and its poles (Gönczy et al., 2001). To test its association with the astral microtubules, we generated three strains by CRISPR-Cas9: one with fluorescently-labelled ZYG-8 endogenously expressed, mNG::ZYG-8; a second with *zyg-8* tagged at the locus with three OLLAS tags; and a third with an integrated transgene that overexpresses *zyg-8* (*pPie-1*::mNG::3*OLLAS::ZYG-8) on top of the endogenous copy (Table S1). During the first embryonic division of endogenously expressed and overexpressed *zyg-8* strains, ZYG-8 significantly co-localised with tubulin on astral and spindle microtubules (Figure S1, Method M5). We concluded that ZYG-8 localisation was consistent with its potential role in regulating microtubule flexural rigidity.

To change the amount of ZYG-8 in the embryo, we altered its expression level by performing RNAi against *zyg-8* or by over-expressing it. Western blot analysis of worm lysates showed decreased or increased OLLAS levels, respectively (Figure S2A-B, Method M6). Additionally, we found corresponding changes in mNG::ZYG-8 fluorescence on both spindle and astral microtubules in zygotes (Figure S2-CD, Method M6). These results validated that we could vary the amount of ZYG-8 bound to microtubules, providing an effective means to assess its role in controlling microtubule rigidity.

Next, we explored ZYG-8 potential role in regulating microtubule rigidity in the nematode zygote. To do this, we examined the shapes of the astral microtubules as a proxy similar to previous work in the axonal growth cone (Jean et al., 2012). We imaged the microtubules by immunostaining in fixed embryos using a confocal super-resolved microscope. We observed more bent microtubules in the RNAi-treated embryos (Figure 1C, G compared to A, E). To further test the effect seen by RNAi, we studied the thermosensitive mutant, *zyg-8(or484ts)*, which carries a mutation in the first doublecortin domain (Gönczy et al., 2001; Wood et al., 1980). This mutant has been previously reported to prevent ZYG-8 binding to microtubules at the restrictive temperature of 25°C (Bellanger et al., 2007). In the mutants, we observed even larger curvatures along the microtubules at the restrictive temperature (Figure 1 D, H compared to B, F). During anaphase, we also noticed fragmented microtubules within the

cytoplasm of some mutant embryos (Figure 1H). Taken together, the changes in microtubule shape upon *zyg-8* targeting suggested a role in regulating microtubule rigidity.

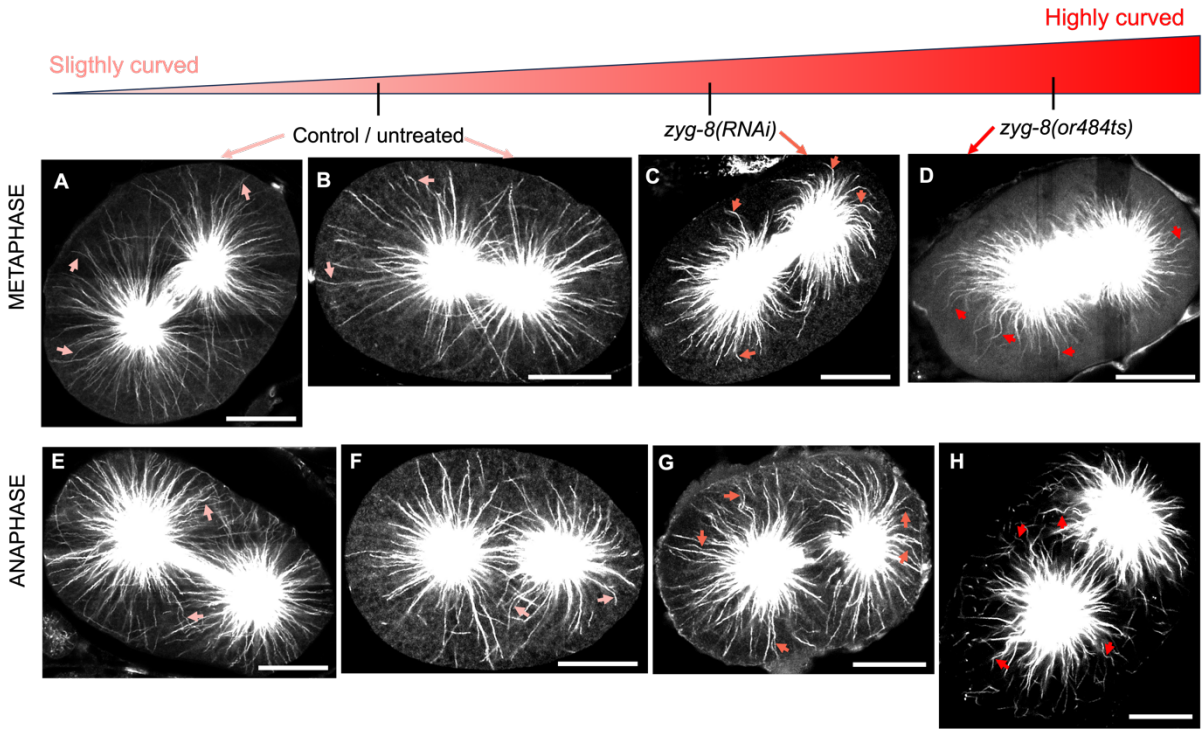

Figure 1: Astral microtubules appear more curved upon targeting *zyg-8*.
(**A-H**) The deconvolved confocal images of fixed embryos with α-tubulin immunostaining reveal microtubule shapes during (A-D) metaphase or (E-H) anaphase in various conditions: (A, E) control embryos, (B, F) untreated embryos at the restrictive temperature, (C, G) *zyg-8(RNAi)* treated embryos, and (D, H) *zyg-8(or484ts)* mutant embryos at the restrictive temperature (Methods M3 and M4). Coloured arrowheads indicate high local curvatures. The scale bars represent 10 μm.

To go beyond this visual inspection, we set out to quantify the curvature distribution of the microtubules. Indeed, measuring microtubule rigidity in *C. elegans* embryos cannot be performed using usual *in vitro* methods (e.g. thermal fluctuations, optical trap/tweezers, calibrated flow) (Felgner et al., 1997; Felgner et al., 1996; Gittes et al., 1993; Kikumoto et al., 2006; Kurz and Williams Jr, 1995; Mickey and Howard, 1995; Venier et al., 1994). As an alternative, comparing the distributions of microtubule local curvatures has been previously performed (Bicek et al., 2009; Blob et al., 2023; Zhang et al., 2017). Assuming that the forces applied to the microtubule network are similar between the two studied conditions, a distribution displaying a larger proportion of highly curved microtubules would reflect a lower microtubule rigidity. It, however, requires segmenting the microtubules. The challenge lies in the faint and uneven labelling of microtubules. To tackle it, we assembled a dedicated image processing pipeline in five steps, which allowed us to segment the astral microtubules and then calculate their local curvatures on a pixel-by-pixel basis and using a three-point method (Figure S3, Method M7). By generating the averaged curvature distribution for each condition, we observed a slight increase in the proportion of high local curvatures following *zyg-8(RNAi)* treatment (Figures 2A-B & S4). The local curvature distribution of *zyg-8(or484ts)* mutants at the restrictive temperature was significantly different from that of untreated embryos. It showed a more pronounced shift toward higher curvatures than the RNAi treatment (Figures 2C-D & S5). We then focussed on the 95th percentile curvature per microtubule as an indicator of the highest curvature. By measuring the median of the highest curvatures (95th percentile)

for each z-projected section, we found mild increases for *zyg-8(RNAi)* and large increases in the mutants (Figure 2E-F). Investigating microtubule curvatures suggested that microtubules were less rigid upon *zyg-8(RNAi)* and even softer in *zyg-8(or484ts)* mutants at the restrictive temperature.

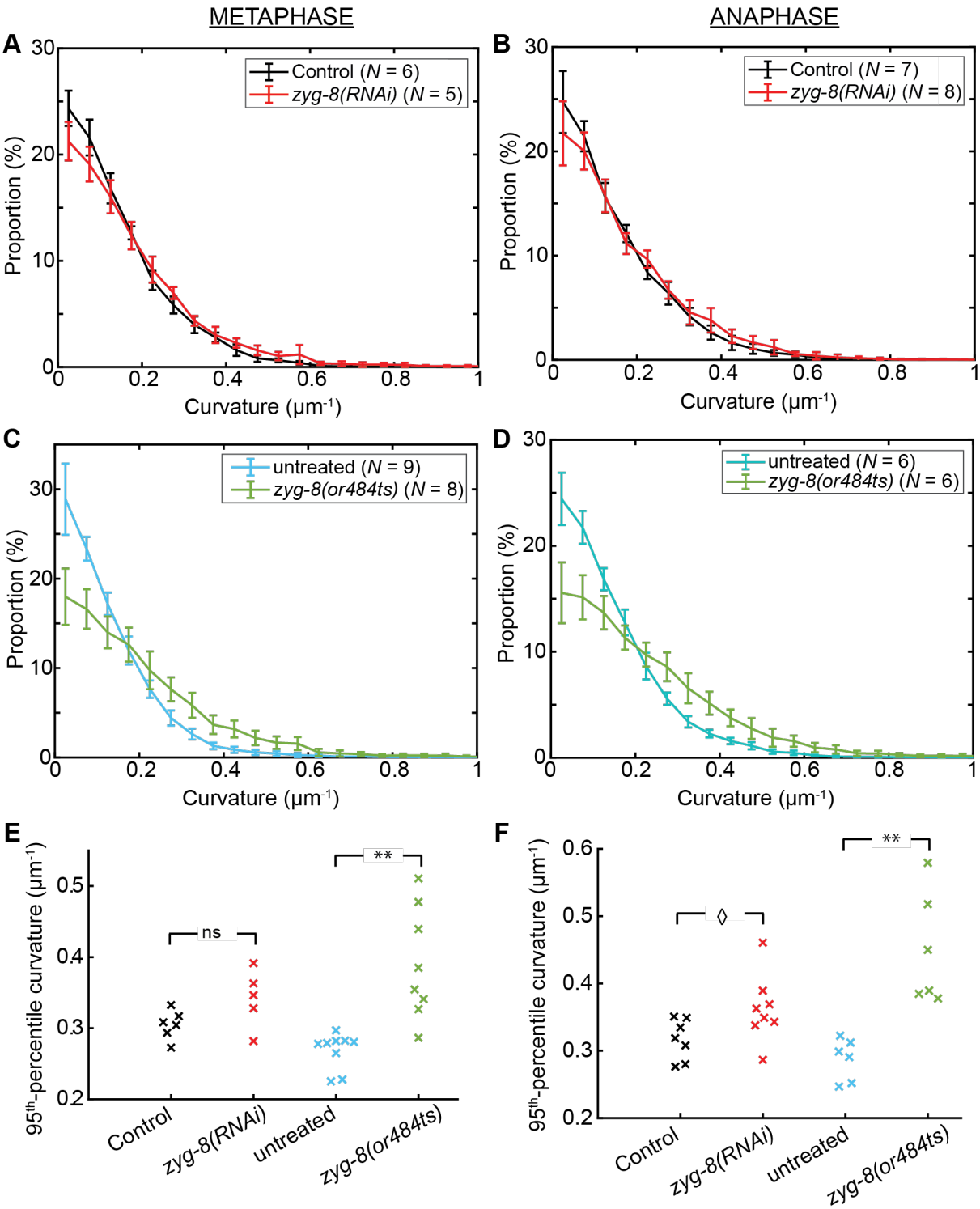

Figure 2: Upon targeting *zyg-8*, the proportion and magnitude of microtubule curvatures are increased.

(**A-B**) Local curvatures of the astral microtubules of (red) *zyg-8(RNAi)* treated embryos and (black) control embryos: (A) during metaphase with (red) *N* = 5 z-projected sections and (black) *N* = 6 z-

projected sections (Kolmogorov–Smirnov test: p = 0.36, Method M14); and (B) during anaphase with (red) N = 8 z-projected sections and (black) N = 7 z-projected sections (Kolmogorov–Smirnov test: p = 0.36, Method M14). **(C-D)** Local curvatures of the astral microtubules of (light green) *zyg-8(or484ts)* mutants and (light blue) untreated embryos, both at the restrictive temperature: (C) during metaphase with (light green) N = 8 z-projected sections and (light blue) N = 9 z-projected sections (Kolmogorov–Smirnov test: p = 0.03, Method M14); and (D) during anaphase with (light green) N = 6 z-projected sections and (light blue) N = 6 z-projected sections (Kolmogorov–Smirnov test: p = 0.014, Method M14). (**E-F**) Medians per z-projected section of the highest curvatures (measured as 95th percentile curvature): (E) during metaphase (data are the same as for (A, C)) and (F) during anaphase (data are the same as for (B, D)). Embryos were fixed, immune-stained for α-tubulin, and curvatures were extracted (Methods M3, M4, M7 & M14).

We sought a complementary quantification of microtubule shape deformation that does not depend on curvature computation. Indeed, the latter may be sensitive to the microtubule sampling. We proposed characterising the astral microtubules' tortuosity (Figure 3A) (Nishida et al., 2023). Interestingly, we observed a significantly greater tortuosity following *zyg-8(RNAi)* treatment. It was even more pronounced in *zyg-8(or484ts)* mutants at the restrictive temperature (Figure 3B-C). Taken together, by studying astral microtubule shapes, we found that ZYG-8 controls microtubule curvatures and tortuosity, suggesting that ZYG-8 regulates microtubule flexural rigidity.

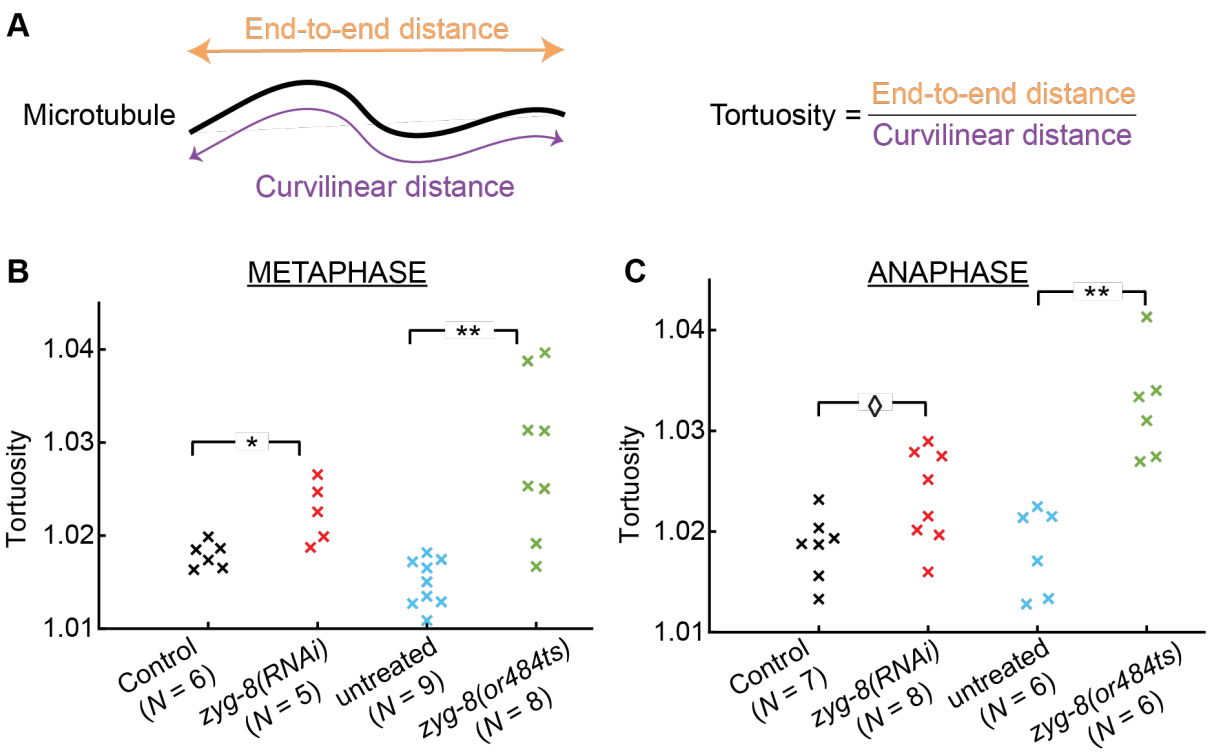

Figure 3: Astral microtubule tortuosity increases upon targeting *zyg-8*.
(A) Schematic about microtubule tortuosity measured as the ratio of curvilinear-distance over end-to-end distance. (**B-C**) Medians per z-projected section of microtubule tortuosities: (B) during metaphase using the same embryos as for Figure 2A, C, E and (C) during anaphase using the same embryos as for Figure 2B, D, F (Methods M7 and M14).

2- ZYG-8 controls the cortical contact durations of astral microtubules through their flexural rigidity.

We, along with others researchers, have recently suggested that microtubule pushing against the cell cortex contributes to centring the spindle in metaphase and that microtubule buckling increases the stability of that process (Bouvrais et al., 2021; Garzon-Coral et al., 2016; Pécréaux et al., 2016). We reckoned that decreasing microtubule flexural rigidity would diminish the pushing exerted by each buckled microtubule (Euler force), consequently increasing its lifetime at the cortex (Brun et al., 2009; Janson et al., 2003). We first used the established agent-centred simulation *Cytosim* to test this hypothesis by varying microtubule rigidity (Figure S6A, Table S2, Movies S1-S3, Method M8) (Nedelec and Foethke, 2007). Similar to what we observed in *zyg-8(RNAi)* and *zyg-8(or484ts)* mutants, we found that both the highest microtubule curvatures (95th percentile) and the microtubule tortuosity increased when microtubule rigidity decreased (Figure S6B-C). Importantly, we measured that cortical lifetimes were increased when microtubule rigidity was reduced (Figure S6D). Thus, *in silico* analysis validated our hypothesis and showed that varying microtubule rigidity was enough to affect oppositely astral microtubule cortical lifetimes.

We next measured the cortical contact durations of the astral microtubules *in vivo* (Bouvrais et al., 2021; Bouvrais et al., 2018) (Method M9). We found a significant increase in the contact durations upon *zyg-8(RNAi)* during metaphase (Figure 4A-C). Conversely, *zyg-8* overexpression led to slightly shorter contact durations than untreated embryos (Figure 4D-F). These duration variations were consistent with ZYG-8 rigidifying the microtubules. Overall, we found that targeting *zyg-8* affected the microtubule rigidity, leading to cortical lifetimes of astral microtubules that vary inversely with their rigidity.

Our previous work demonstrated that cortical lifetime variations could also result from perturbing microtubule dynamics (Bouvrais et al., 2021). As the Doublecortin family may regulate microtubule growth in certain conditions (Bellanger et al., 2007; Lin et al., 2000; Srayko et al., 2005), we assessed whether astral microtubule growth rate was altered upon *zyg-8* targeting using an EB-labelling of their plus-ends (Method M10). In *zyg-8(or484ts)* mutants at the restrictive temperature, we observed a significant reduction of 16% (Figure S7A), similar to the previous *zyg-8(RNAi)* depletion through injection (Srayko et al., 2005). However, we found no significant change upon *zyg-8(RNAi)* or *zyg-8* overexpression (Figure S7B, C). The latter observations suggested that increased or decreased cortical lifetimes upon *zyg-8(RNAi)* treatment or *zyg-8* overexpression cannot be explained by a significant variation in the microtubule growth rate.

Longer durations of cortical microtubule contacts could also originate from more astral microtubules reaching the cortex, thus reducing the force born by each of them. Besides, a slight nucleation rate increase has been previously observed following *zyg-8(RNAi)* treatment through injection (Srayko et al., 2005). We thus counted the comets emanating from the centrosomes using an EB-labelling to investigate the nucleation rate (Method M10). We measured a mild increase of the nucleation rate with *zyg-8(or484ts)* mutants and a mild decrease upon *zyg-8* overexpression, while no significant change in the nucleation rate was found upon *zyg-8(RNAi)* (Figure S8A-C). As the diameter of the centrosome is associated with its nucleation power (Baumgart et al., 2019; Decker et al., 2011; Piehl et al., 2004), we also measured the diameters of fluorescently labelled centrosomes using mCherry::TBG-1 (Method M12). We found a significant diameter decrease upon *zyg-8* overexpression (Figure

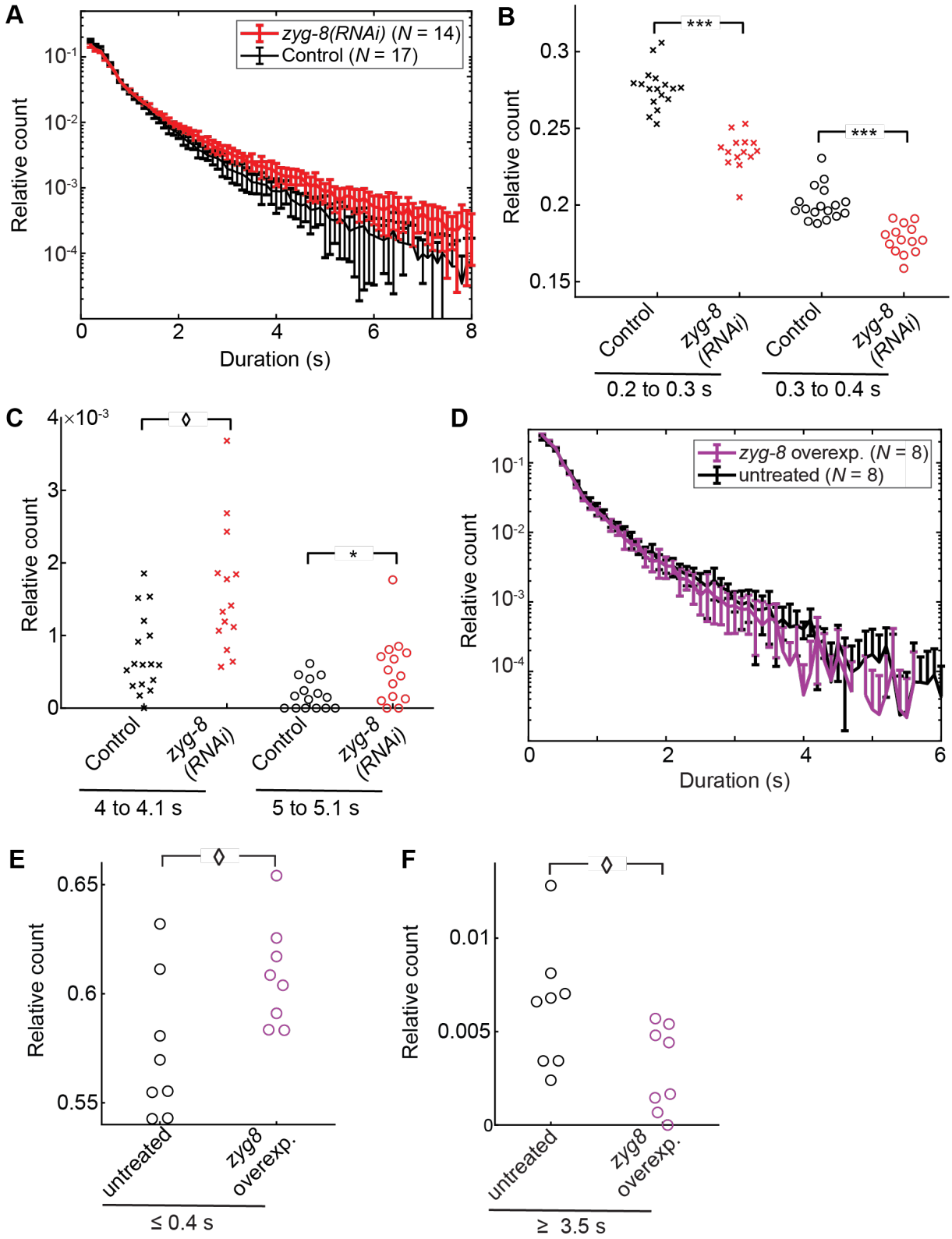

Figure 4: Cortical lifetimes of astral microtubules in metaphase anticorrelate with ZYG-8 expression level.

(**A**) Embryo-averaged and normalised distributions of the cortical lifetimes of astral microtubules during metaphase. We tracked and analysed the cortical contacts of microtubules labelled by GFP::TBB-2: (red) N =14 *zyg-8(RNAi)* treated embryos and (black) N = 17 control ones (Kolmogorov–Smirnov test: $p = 6\times10^{-4}$, Methods M9 and M14). (**B-C**) Relative counts for (B) the two lowest durations (0.2 s & 0.3 s) and (C) two longer durations (4 & 5 s) of the distributions presented in (A) to highlight

variations in the relative counts of the shortest durations or the longest ones (Method M14). (**D**) Embryo-averaged and normalised distributions of the cortical lifetimes of astral microtubules during metaphase. We tracked and analysed the cortical contacts of microtubules labelled by mCherry::tubulin: (purple) N = 8 *zyg-8* overexpressing embryos and (black) N = 8 untreated ones (Kolmogorov–Smirnov test: p = 0.18, Methods M9 and M14). (**E-F**) Relative counts for (E) the durations below 0.4 s and (F) the durations above 3.5 s of the distributions presented in (D) to highlight variations in the relative counts of the shortest and longest durations (Method M14).

S8D). We also observed a slight diameter increase following *zyg-8(RNAi)* treatment (Figure S8E). Comparatively, a mild depletion of SPD-2^{CEP192} led to a much larger reduction in centrosome diameter (Figure S8F) (Woodruff et al., 2015). Overall, our measurements confirmed that ZYG-8 limits the microtubule nucleation rate, although to a lower degree. Consequently, we proposed that the variations in microtubule cortical contact durations upon targeting *zyg-8* cannot be explained by the sole mild perturbation of the microtubule nucleation rate. Accounting for the perturbation of microtubule flexural rigidity enabled to explain the changes in microtubule cortical contact durations upon targeting *zyg-8*.

From a functional standpoint, ZYG-8 regulates the flexural rigidity of astral microtubules, influencing their cortical residence times and likely playing a key role in proper spindle positioning.

3- **ZYG-8 regulates the centring force through microtubule rigidity.**

We foresaw that we could target *zyg-8* to reveal the contribution(s) of microtubule rigidity in spindle positioning during anaphase. Indeed, centring force, mostly invoked in metaphase, depends essentially on the microtubule rigidity (Bouvrais et al., 2021; Garzon-Coral et al., 2016; Pécréaux et al., 2016). This force is also expected to serve as restoring force during the rocking of the spindle in anaphase (Grill et al., 2005; Pécréaux et al., 2006a). Upon *zyg-8(RNAi)*, we observed a large increase in the spindle-pole oscillation amplitudes (Figure 5A, Method M11). Interestingly, we also noticed a significant reduction in the frequency of these oscillations, consistent with softer microtubules (Figure 5B) (Howard, 2006; Pécréaux et al., 2006a). We considered two potential, non-exclusive mechanisms for the increased oscillation amplitudes: enhanced cortical pulling or reduced cortical pushing. First, we measured the most-posterior position of the posterior centrosome during anaphase following *zyg-8(RNAi)* treatment and found no significant difference, suggesting that the anaphase cortical pulling force was not substantially altered (Figure S9). Next, we applied the DiLiPop analysis to examine the cortical contact durations of astral microtubules during anaphase to assess cortical pulling and pushing events (Bouvrais et al., 2021) (Method M9). For the pulling events, we observed a modest rise in their lifetime by 10% and a slight reduction in their density by 3% (Figure 5C). Since all cortical force generators are engaged in pulling events during anaphase, the reduced density following *zyg-8(RNAi)* treatment likely reflected the longer duration of each pulling event (Bouvrais et al., 2018; Grill and Hyman, 2005). We concluded that *zyg-8(RNAi)* treatment did not significantly affect the cortical pulling force. In contrast, we found that pushing microtubules resided at the cortex for a longer duration (+37%) upon *zyg-8(RNAi)*, which aligned with their dependence on microtubule rigidity (Figure 5D1). Besides, we observed a significant increase in the density of pushing events by 22%, likely due to the nucleation rate increase (Figure 5D2). We proposed that the larger oscillation amplitudes seen following *zyg-8(RNAi)* treatment resulted from reduced cortical pushing

force, despite the rise in pushing event density. We attributed this force reduction to softer microtubules, leading to less efficient pushing events.

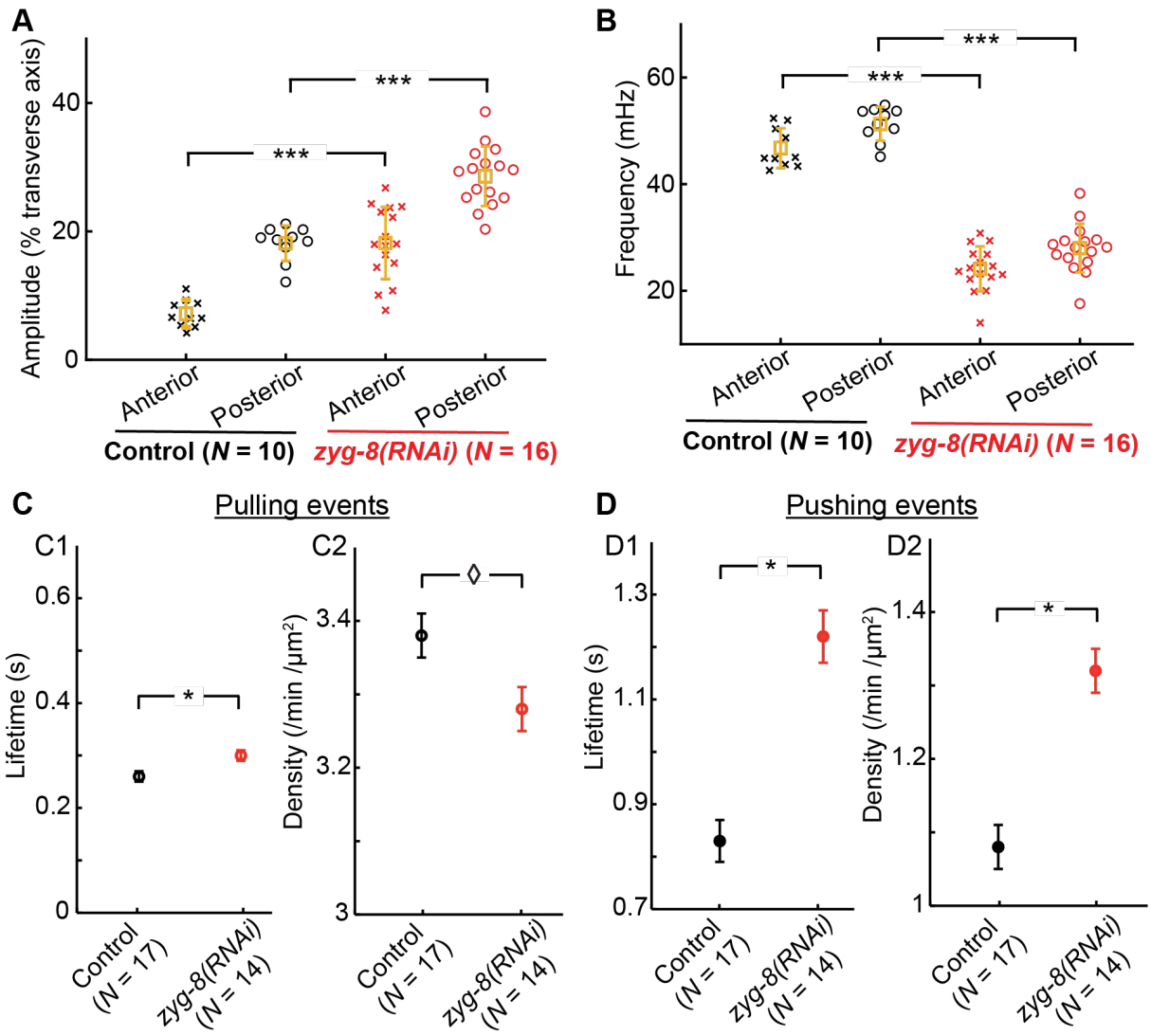

Figure 5: Depleting ZYG-8 increases oscillation amplitudes.
(**A**) Maximal peak-to-peak amplitudes of spindle pole oscillations and (**B**) frequencies of the oscillations. We tracked and analysed the centrosomes labelled by GFP::TBB-2: (red) *N* = 16 *zyg-8(RNAi)* treated embryos and (black) *N* = 10 control embryos (Method M11). The orange squares and error bars correspond to the means and SD (Method M14). (**C**) Lifetimes and densities of the cortical pulling events, and (**D**) lifetimes and densities of the cortical pushing events. We tracked and analysed the microtubule contacts at the cell cortex using a GFP::TBB-2 fluorescent labelling: (red) *N* = 14 *zyg-8(RNAi)* treated embryos and (black) *N* = 17 control embryos (same embryos as in Figure 4A-C) (Methods M9 & M14).

We sought an alternative characterisation of spindle positioning forces at the cellular level to ascertain ZYG-8 role in changing microtubule rigidity and centring force generated by microtubules pushing against the cortex. To do this, we extracted the mechanical fingerprint of spindle positional micro-movements along the transverse axis during anaphase and fitted the experimental spectrum to a second-order model (Pécréaux et al., 2016) (Method M13). Our results showed that ZYG-8 depletion led to a large reduction in the centring-to-damping corner frequency f_c, which decreased by 61% compared to the control (Table S3). We also

observed a decrease in the diffusion coefficient *D* (scaling inversely to damping) by 29% and an increase in the damping-to-inertia frequency f_0, which rose by 53% (Table S3). We interpreted the decrease in f_c as primarily reflecting a centring force reduction (Pécréaux et al., 2016). The modest change in *D* was likely due to more microtubules contacting the cortex. f_0 increase would be partly due to the reduced *D*, but appeared hardly compatible with any increase in inertia. It suggested that the pulling forces were only mildly or not affected. Overall, the spindle positional mechanical fingerprint following *zyg-8(RNAi)* treatment was qualitatively consistent with a reduction in the centring force, likely due to softer microtubules.

Next, we investigated whether *zyg-8* overexpression would affect spindle pole oscillation. We observed no significant variation in the maximal amplitudes, but there was a significant increase in oscillation frequency, consistent with stiffer astral microtubules (Figure S10A-B). Additionally, we found no change in the most-posterior position of the posterior centrosome (Figure S10C). Using the DiLiPop assay, we revealed upon *zyg-8* overexpression that the lifetime of pulling events was not significantly affected, and their density was slightly reduced (Figure S10D). Both sets of experiments suggested that the cortical pulling force was not significantly altered by *zyg-8* overexpression. In terms of pushing events, DiLiPop analysis revealed a slight reduction in their lifetime, with no change in their density (Figure S10E). We also studied spindle positional micro-movements along the transverse axis in *zyg-8* overexpressing embryos during anaphase. Fitting the experimental spectrum of these micro-movements suggested no major change in centring-to-damping corner frequency, indicating that centring efficiency was unaffected by *zyg-8* overexpression (Table S3). Altogether, the DiLiPop analysis and the positional micro-movements study indicated no substantial variation in the cortical pushing/centring forces upon *zyg-8* overexpression, consistent with the unaffected spindle pole oscillation amplitudes. Therefore, we proposed that either the increase in microtubule rigidity upon *zyg-8* overexpression was not large enough to have a functional impact, or that this increase was effectively compensated.

Given that we observed a modest regulation of microtubule nucleation by ZYG-8, we questioned to what extent this could contribute to the phenotypes described above. To do so, we compared the mechanical fingerprint of spindle positional micro-movements during anaphase upon *zyg-8* overexpression and SPD-2^{CEP192} depletion, as both treatments are known to reduce the nucleation rate (Srayko et al., 2005). We performed a mild *spd-2(RNAi)*, leading to a more significant reduction in centrosome diameter than *zyg-8* overexpression (Figure S8D, F). When we fitted the experimental spectrum of the spindle transverse positional micro-movements in the *spd-2(RNAi)* condition, we found an increase in *D* and f_c, in contrast to the effects of *zyg-8* overexpression (Table S3). Based on these results, we proposed that the differences observed in the mechanical parameters upon *zyg-8* overexpressing were likely driven by an increase in microtubule rigidity, rather than by changes in the nucleation rate. Similarly, we suggested that this rate only modestly contributed to *zyg-8(RNAi)* mechanical fingerprint phenotype.

Altogether, our results showed that ZYG-8 regulated the cortical pushing force, also called the centring force. This force acted as a restoring force during anaphase spindle rocking, primarily by controlling microtubule flexural rigidity. Our work highlighted that this force contributed to spindle choreography, although cortical pulling forces, which drive the spindle posterior displacement, remain dominant.

4- Very soft microtubules cause strong defects in spindle final positioning and orientation.

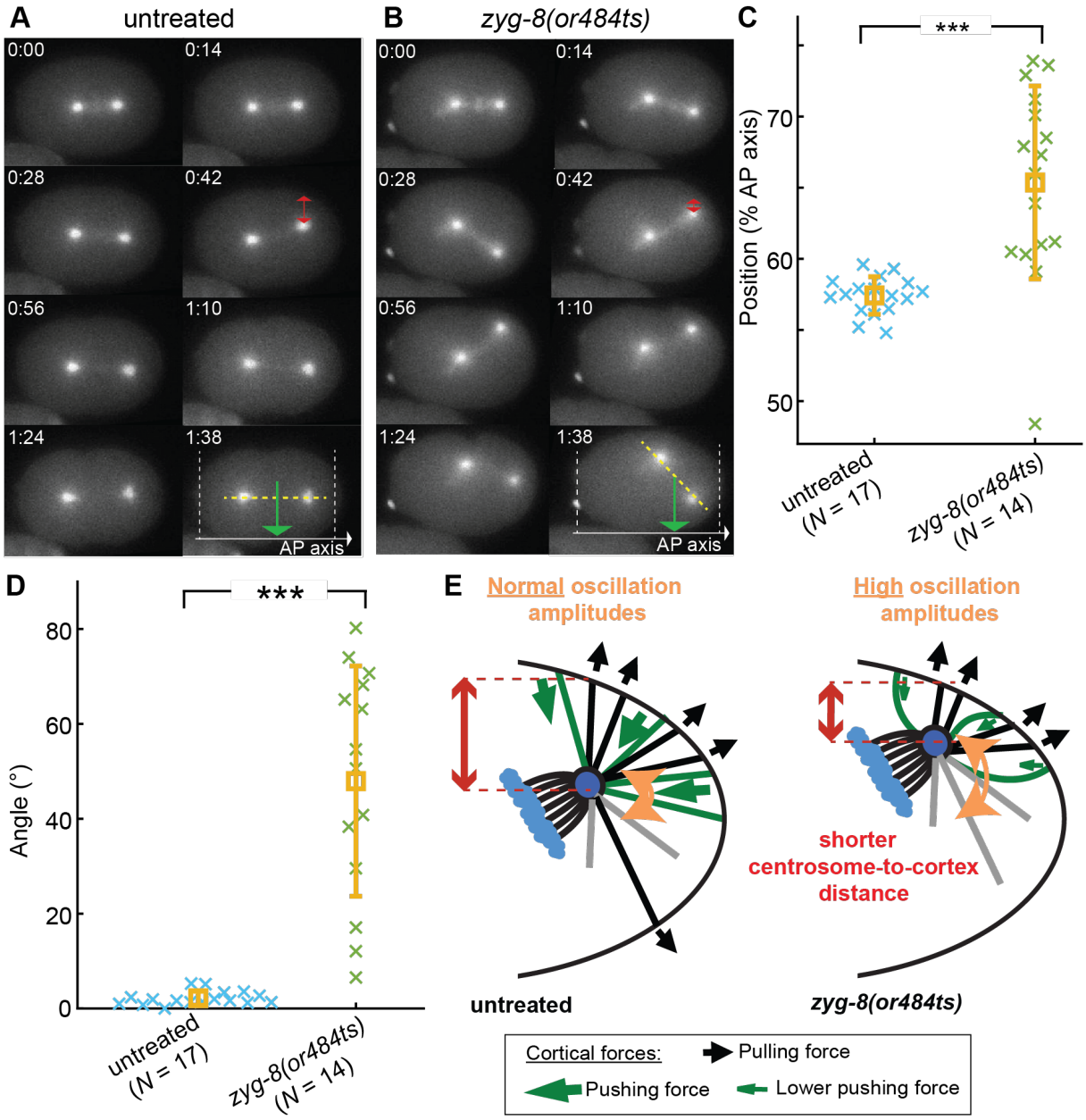

Figure 6: In *zyg-8(or484ts)* mutants, overly soft microtubules result in a misoriented and mispositioned spindle at the anaphase end.

(**A-B**) Time-lapse series of (A) an exemplar untreated embryo and (B) an exemplar *zyg-8(or484ts)* mutant along anaphase, both at the restrictive temperature and with EBP-2::mKate2 labelling. The green arrows indicate the spindle's final positions along the anteroposterior (AP) axis and the dotted yellow lines indicate the final orientations. The red double-headed arrows underline the minimal centrosome-to-cortex distances. The scale bars represent 10 µm. (**C-D**) Spindle final (C) positions along the AP axis and (D) angles for (light green) N = 14 *zyg-8(or484ts)* mutants and (light blue) N = 17 untreated embryos, both at the restrictive temperature. We tracked and analysed the centrosomes labelled by EBP-2::mKate2 (Method M11). The orange squares and error bars correspond to the means and SD (Method M14). (**E**) Schematics illustrating how a large reduction in microtubule flexural rigidity could lead to spindle positioning and orientation defects.

After revealing a novel role for ZYG-8 in controlling microtubule flexural rigidity, we investigated its relevance to mitosis success. Interestingly, in *zyg-8(or484ts)* mutants at the restrictive temperature, we observed larger spindle pole oscillation amplitudes compared to the *zyg-8(RNAi)* treatment (Figure S11). We attributed this phenotype to weakened centring caused by overly soft microtubules, which was supported by a larger reduction in the centring-damping corner frequency f_c and increased proportion and magnitude of microtubules curvatures (Table S3, Figures 2 and 3). It resulted in a significantly reduced centrosome-to-cortex distance. We thus explored the consequences of this reduced distance in the course of anaphase. In untreated embryos, oscillations progressively build up and then die down, leaving the spindle aligned along the embryo anteroposterior (AP) axis (Figure 6A). However, in *zyg-8(or484ts)* mutants at the restrictive temperature, the centrosome's proximity to the cell periphery pulled the entire spindle further toward the cell cortex and seemed to interrupt the oscillation die-down incorrectly (Figure 6B). Reduced pushing, along with proximity to the cortex, both disrupt the force balance, favouring excessive pulling (Bouvrais et al., 2018). As a result, the spindle could not return to the central position at the anaphase end, leading to mispositioning and misorientation (Figure 6B-D). Based on these observations, we proposed that misoriented spindle at the anaphase end in *zyg-8(or484ts)* mutant were due to impaired pushing forces.

We tested the hypothesis that microtubule rigidity perturbation contributed to spindle misorientation and mispositioning in *zyg-8(or484ts*) mutants. A previous and alternative explanation suggested that these defects in the mutants could be due to very short astral microtubules that failed to reach the opposite cortex (Bellanger et al., 2007; Gönczy et al., 2001). This was supported by observations of very short astral microtubules in fixed *zyg-8(or484ts)* mutant stained with anti-tubulin at the anaphase stage. However, in our experiments, we observed this prominent phenotype in only a small fraction of fixed mutants (33%). To safeguard against possible artefacts, especially given that the reduced microtubule rigidity might make them more fragile to fixing, we imaged live embryos labelled with GFP::TBB-2. In *zyg-8(or484ts)* mutants at the restrictive temperature, we observed exaggerated rocking during anaphase. At the end of mitosis, the spindle was positioned more posteriorly and tilted (Movies S4 and S5 compared to Movie S6 for control). Interestingly, the astral microtubules were long enough to reach the cell periphery, even during anaphase spindle pole oscillations (Figure S12A, Movies S4&S5). Based on these observations, we proposed that the positional defects observed in *zyg-8(or484ts)* mutants at the restrictive temperature were caused by overly soft microtubules rather than too-short microtubules.

In conclusion, sufficiently rigid microtubules were essential to generate enough centring force in anaphase to prevent the centrosome from being displaced too far from the centre and ensure proper final orientation (Figure 6E). This reproducible spindle displacement guaranteed the correct partitioning of cell fate determinants.

5- PTL-1, like ZYG-8, reduced the centring forces, although to a lower extent.

Since ZYG-8 has been involved in other functions during cell division, we set out to target another protein known to regulate microtubule flexural rigidity in neurons and test whether we could reproduce similar perturbations in spindle choreography. We depleted the sole nematode homolog of the Tau family, PTL-1, using RNAi (Goedert et al., 1996; McDermott et al., 1996). We measured a modest increase in the maximal amplitudes of spindle pole

oscillations and a reduction in their frequencies, consistent with softer microtubules (Figure 7). Besides, when examining the spindle positional micro-movements along the transverse axis during anaphase, we found that the centring-damping corner frequency f_c was reduced (Table S3). These results closely resembled those obtained with *zyg-8(RNAi),* suggesting a reduction in centring forces, albeit to a lesser degree. These weaker phenotypes observed might be explained by the low levels of *ptl-1* expression in the zygote compared to *zyg-8* (Tintori et al., 2016). Based on these findings, we proposed that PTL-1 also controlled microtubule flexural rigidity and contributed to spindle choreography during *C. elegans* zygote division. Furthermore, our results with PTL-1 reinforced the crucial role of ZYG-8 in controlling microtubule flexural rigidity to ensure proper spindle positioning and orientation.

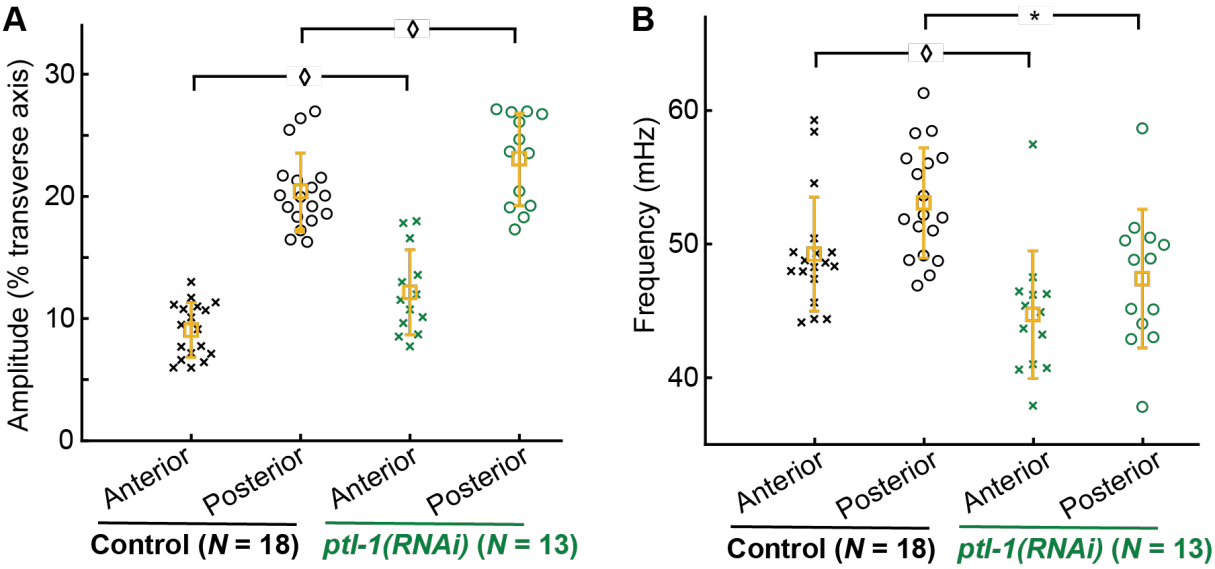

Figure 7: *ptl-1(RNAi)* leads to larger spindle pole oscillation amplitudes during anaphase, similar to *zyg-8(RNAi)*, although to a lesser extent.
(**A**) Maximal amplitudes of spindle pole oscillations and (**B**) frequencies of the oscillations for (green) *N* = 13 *ptl-1(RNAi)* treated embryos and (black) *N* = 18 control embryos. We tracked and analysed the centrosomes labelled by mCherry::TBG-1 (Method M11). The orange squares and error bars correspond to the means and SD (Method M14).

DISCUSSION

Our work proposes that ZYG-8 is a major player in *C. elegans* mitosis, mainly through rigidifying the microtubules. This contribution is crucial for generating cortical pushing forces large enough to counteract the intense cortical pulling forces during anaphase. Proper force balance during anaphase ensures accurate spindle orientation at the end of mitosis.

Previous research on mitotic spindle positioning in the *C. elegans* zygote has highlighted the crucial roles of asymmetric cortical pulling forces controlled by PAR polarity, and microtubule dynamics (Bouvrais et al., 2021; Bouvrais et al., 2018; Fielmich et al., 2018; Grill et al., 2001; Grill et al., 2003; Kozlowski et al., 2007; Nguyen-Ngoc et al., 2007; Pécréaux et al., 2016; Redemann et al., 2010; Wu and Rose, 2007). Besides, cortical pushing forces have been proposed as centring forces during metaphase (Garzon-Coral et al., 2016; Pécréaux et al., 2016). The current study complements, and also departs from, these previous investigations.

Firstly, it reveals that controlling microtubule flexural rigidity participates in spindle choreography. Particularly, this control avoids excessive closeness of the spindle poles to the cell periphery during anaphase. We indeed observed increased spindle pole oscillation amplitudes following ZYG-8 or PTL-1 depletion (Figures 5A & 7A). This microtubule rigidity control is complementary to the well-known regulation by microtubule dynamics. Secondly, our study underlines that cortical pushing force also contributes to spindle positioning during anaphase, although cortical pulling forces are dominant and their asymmetry ensures spindle posterior displacement (Grill et al., 2003; Nguyen-Ngoc et al., 2007). It is often assumed that the cortical pushing force plays little to no role due to the comparatively high intensity of cortical pulling forces and the reduced level of cortical pushing forces caused by microtubule buckling (Dogterom et al., 2005; Farhadifar et al., 2020; Wu et al., 2021). We propose that weakening the cortical pushing forces, as observed in *zyg-8(or484ts)* mutants, hinders the spindle's return to the anteroposterior axis (Figure 6B). This disruption precludes the correct final position and orientation of the spindle, ultimately affecting the accurate segregation of fate-determining factors (Figure 6C-D). Importantly, our previous work highlighted a steep increase in the cortical pulling force below a centrosome-to-cortex threshold distance (Bouvrais et al., 2018). Here, we show that astral microtubules in *zyg-8(or484ts)* mutants are capable of contacting the opposite cortex (Figure S12, Movies S1 and S2), which differed from Kozlowski work suggesting that limited access of astral microtubules to the cell cortex caused spindle oscillation (Kozlowski et al., 2007). This observation rules out a mechanism grounded on limited cortical access by the microtubules. Overall, the astral microtubule network functions like a spring, restricting the spindle transverse motion away from the centre in *C. elegans* zygotes (Garzon-Coral et al., 2016; Howard, 2006; Pécréaux et al., 2016). Therefore, microtubule flexural rigidity emerges as a critical physical parameter in controlling the intensity of centring force.

Our results suggest an essential role for pushing, although this force is dominated by pulling. We foresee that our finding goes beyond the nematode's first division and may be relevant to other asymmetric divisions and maybe further. It is well established that the pulling dominates the spindle orientation. It is accounted for by the canonical model based on the molecular machinery composed of the cortical $G\alpha$-LGN^{GPR}-$NuMA^{LIN-5}$ complex and the cytoplasmic dynein motor (Bergstralh et al., 2017; di Pietro et al., 2016). However, less attention has been paid to spindle orientation, which relies on the cortical pushing forces. The dependence of spindle orientation on cell shape, which is often neglected, suggests that the pushing force could play a significant role in this process (Jingchen et al., 2019; Mao et al., 2011; Singh et al., 2021; Strauss et al., 2006; Tsou et al., 2002). In other systems, some studies found that the spindle did not align with the dynein-enriched cortical zones (Izumi et al., 2006; Saleh et al., 2023; Siller et al., 2006; Williams et al., 2011). Consequently, the traditional canonical model alone cannot account for spindle orientation in various contexts. We propose that the cortical pushing force contributes to this phenomenon and, furthermore, that the flexural rigidity of microtubules must be sufficiently high. Notably, the orientation of the mitotic spindle defines the direction in which a cell divides. Therefore, many developmental processes, ranging from germline stem cell division to epithelial tissue homeostasis and regeneration, require correct mitotic spindle orientation. Deficits in spindle orientation have been associated with various diseases, such as organogenesis and morphogenesis failures, or cancer (Baena-López et al., 2005; Fededa et al., 2016; Fischer et al., 2006; Fleming et al., 2009; Gao et al., 2017; Pease and Tirnauer, 2011; Quesada-Hernández et al., 2010; Quyn et al., 2010).

Our study revealed that ZYG-8^{DCLK1} plays a crucial role in regulating the flexural rigidity of microtubules during zygote division, marking a novel function for this protein in mitosis. Looking ahead, it will be intriguing to explore the mechanisms through which ZYG-8 rigidifies the microtubules. Several mechanisms of microtubule rigidification have been proposed— primarily in the context of neurons— and we discuss them in light of our findings. We take advantage of the numerous studies on the DCX protein, which shares the two same microtubule-binding domains as DCLK1^{ZYG-8}. Besides, these two doublecortin domains are highly conserved in ZYG-8 (Gönczy et al., 2001). (1) Microtubules can be rigidified by hindering the sliding of protofilaments through the binding of MAPs across these protofilaments. DCX binding on the microtubules is compatible with this mechanism since it reinforces lateral and longitudinal dimer couplings. (2) Rigidification can also occur by bundling multiple microtubules together. Previous studies revealed such a mechanism for the Doublecortin family *in vitro* and *in vivo* (Bellanger et al., 2012; Bielas et al., 2007; Couillard-Despres et al., 2004; Horesh et al., 1999; Kim et al., 2003; Lin et al., 2000; Moores et al., 2006). In particular, *zyg-8(or484ts)* mutants displayed a perturbed bundle organisation of microtubules in touch receptor neurons (Bellanger et al., 2012). However, in the *C. elegans* zygote, electron microscopy failed to reveal microtubule bundles in the spindle or astral microtubules close to the poles (Redemann et al., 2017). Therefore, we disfavoured such a mechanism. (3) Microtubule rigidity is also regulated through post-translational modifications (PTM) (Nishi et al., 2023; Portran et al., 2017; Robison et al., 2016; Wall et al., 2020; Xu et al., 2017). Notably, a study showed that DCX expression increases tubulin polyglutamylation in neurons (Sébastien et al., 2023). However, the *ttll-4(-);ttll-5(-);ttll-11(-)* triple mutants did not show any defect in embryonic viability, suggesting that microtubule glutamylation levels may not significantly affect the zygote cell division (Chawla et al., 2016). Dedicated investigations would be needed to address the possible contribution of ZYG-8 through PTM. (4) Self-repair of local damages along the microtubule lattice may also help restore the rigidity or stabilise the curved region (Théry and Blanchoin, 2021). Interestingly, the number of microtubule defects is thought to correlate with the microtubule growth rate (Chrétien et al., 1992; Schaedel et al., 2019), which is particularly high in nematodes (Chaaban et al., 2018). If a high occurrence of holes exists in the *C. elegans* embryo, ZYG-8 could contribute to healing as the Doublecortin family also acts as tubulin oligomer chaperones (Manka and Moores, 2020). However, to date, there has been no evidence of microtubule lattice defects in *C. elegans* zygote. For example, embryos labelled with EBP-2 fluorescence did not show stationary fluorescent spots along the astral microtubules. The various mechanisms proposed above, in which ZYG-8 could play a key role in regulating microtubule flexural rigidity, are not mutually exclusive; several of them may be combined. ZYG-8 rigidifying the microtubule by coupling the protofilaments appears to us the most plausible mechanism currently.

From a broader perspective, we propose a dual role of ZYG-8^{DCLK1} during mitosis, acting by regulating both microtubule rigidity and dynamics. Our research has corroborated Srayko's findings that ZYG-8 enhances microtubule growth while limiting the nucleation of astral microtubules in *C. elegans* zygote (Figures S7 and S8) (Srayko et al., 2005). The present study further emphasises that, upon *zyg-8(RNAi)*, the spindle choreography phenotypes were mainly caused by the disturbed microtubule rigidity, rather than the modest changes in microtubule dynamics. We thus discuss the greater role of ZYG-8 in regulating the flexural rigidity of the microtubule lattice, as opposed to influencing microtubule dynamics at their ends. This is likely because ZYG-8 and EB are thought to compete for the same microtubule binding site at the corner of four tubulin dimers (Fourniol et al., 2010; Manka and Moores,

2018; Maurer et al., 2012). However, EB binds preferentially to the GTP cap at growing ends (Maurer et al., 2012), while Doublecortin family proteins bind *in vitro* to the whole lattice, including microtubule ends (Bechstedt and Brouhard, 2012). *In vivo*, DCX was excluded from microtubule ends (Ettinger et al., 2016). A relative exclusion of ZYG-8 from microtubule ends in *C. elegans* zygote could account for the efficiency differences in its dual role. However, it may be particularly relevant in specific cellular contexts where other proteins necessary for microtubule growth or nucleation are absent or present in low quantities. For example, γ-tubulin ring complexes (γ-TuRCs) may be absent from centrioles or centrosomes in neurons, leading to microtubule nucleation in an acentrosomal manner (Nguyen et al., 2011; Stiess et al., 2010). Interestingly, proteins from the Doublecortin family are highly expressed in neurons, where they regulate microtubule rigidity (Bellanger et al., 2012; Jean et al., 2012). They may also contribute there to microtubule nucleation and/or growth, consistent with their *in vitro* capabilities (Lin et al., 2000; Manka and Moores, 2020; Moores et al., 2004; Moores et al., 2006). Interestingly, collateral branching in hippocampal neurons was significantly delayed following DCX depletion, which may reflect nucleation impairment (Tint et al., 2009). Overall, ZYG-8^{DCLK1} performs multiple microtubule-related functions in a context-dependent manner; we suggest controlling flexural rigidity as a novel one during cell division and possibly beyond.

By uncovering ZYG-8's dual role in *C. elegans* mitosis, we can now question its contribution to zygote meiosis, especially through controlling microtubule flexural rigidity. A recent study highlighted that ZYG-8 promotes meiotic spindle stability and suggested that it may regulate microtubule dynamics and motor-driven forces (Czajkowski et al., 2024). We wonder whether some of the perturbations observed upon targeting *zyg-8* could be attributed to the deregulation of microtubule rigidity. Notably, this study found that most *zyg-8(or484ts)* meiotic spindles were significantly bent at the restrictive temperature. Additionally, some images of the mutant showed microtubules exhibiting high local curvatures. Similar perturbations were also observed following ZYG-8 depletion using the Auxin-inducible degradation system. In light of these observations, it is plausible that ZYG-8 contributes to the assembly or/and stability of meiotic spindles in the zygote by stiffening microtubules.

In conclusion, our findings regarding the pivotal role of ZYG-8^{DCLK1} through stiffening microtubules in spindle positioning and orientation during mitosis offer not only a deeper understanding of the fundamental mechanisms governing cell division but also highlight significant implications for cancer therapy. Given that DCLK1^{ZYG-8} is frequently deregulated in various solid tumours (e.g., those from the colon, pancreas, kidney and breast), this protein is likely involved in a common process such as cell division (Gao et al., 2016; Ge et al., 2018; Ito et al., 2016; Liu et al., 2019). Additionally, as the proteins of the Tau family are also found to be deregulated or mutated in cancers, targeting microtubule rigidity may represent a promising approach for future cancer treatments (Gargini et al., 2019; Papin and Paganetti, 2020; Rossi et al., 2018). This strategy could complement existing therapies targeting microtubule dynamics, which often suffer from side effects and cancer cell resistance.

MATERIAL AND METHODS

M1- C. elegans strains and their culturing

The *C. elegans* strains used in the present study are listed in Table S1. *C. elegans* nematodes were cultured as described in (Brenner, 1974) and dissected to obtain embryos. The strains were maintained at 20°C, except the thermosensitive mutant *zyg-8(or484ts)* maintained at 15°C and AZ244 maintained at 25°C to increase transgene expression. The strains were handled on nematode growth medium (NGM) plates and fed with OP50 *E. coli* bacteria.

M2- RNAi feeding

RNA interference (RNAi) experiments were performed by feeding, as described in (Kamath and Ahringer, 2003). Bacteria were obtained by Source BioScience (*zyg-8* III-6C10; *ptl-1*: III-1A12; *spd-2*: I-4O08). The feedings were performed at 20°C. For *zyg-8* and *ptl-1* RNAi, the treatment lasted 96h and dsRNA expression was induced with 4 mM of IPTG (Isopropyl β-D-1-thiogalactopyranoside). For *spd-2* targeting, the duration was 6h, and dsRNA expression was induced with 1mM IPTG. The control embryos for the RNAi experiments were fed with bacteria carrying the empty plasmid L4440.

M3- Preparation of the embryos for live imaging or immunofluorescence

For the thermosensitive *zyg-8(or484ts)* mutants, we transferred them as L4 larvae to 25°C and incubated for 15 hours before use (Gönczy et al., 2001).

For live imaging, embryos were dissected in M9 buffer (prepared by combining 3 g KH_2PO_4, 6 g Na_2HPO4, 5 g NaCl and 1 mL of 1 M $MgSO_4$ diluted in ultrapure water to 1 L) and mounted on a pad (2% w/v agarose, 0.6% w/v NaCl, 4% w/v sucrose) between a slide and a coverslip.

For immunofluorescence staining, embryos were dissected in M9 buffer and mounted on a slide coated with poly-L-lysine (0.1%) (Sigma-Aldrich P1524). The slides were dipped in liquid nitrogen to crack the embryo's eggshell and immediately transferred to -20°C methanol for fixation for 20 minutes (freeze-cracking method (Duerr, 2013)). They were then rinsed for 10 minutes in PBS 1X before blocking for 20 minutes in PBS-Tween (0.2%) with BSA (1%).

M4- Fluorescence microscopic imaging conditions

The various microscopy setups used are presented in the table below. Embryos were imaged at 23°C, except otherwise stated. Images were stored using the Omero software (Li et al., 2016).

Imaging experiment	**Spindle pole imaging**	**(1) Landing assay to study microtubule cortical contacts; (2) Microtubule dynamics (growth and nucleation rates)**	**(3) Microtubule network, (4) ZYG-8 localisation inside the embryo, (5) microtubule live imaging**
Live or fixed embryo	Live	Live	(3) & (4): Fixed; (5): Live
Microscope type	Zeiss Axio Imager upright	Leica DMi8 equipped with CSU-X1 spinning disk head (Yokogawa)	(3) & (4): Airyscan 2 Zeiss LSM980. (5) Airyscan Zeiss LSM880.
Fluorescent labelling	Spindle poles, e.g. mCherry::TBG-1	(1) Microtubules: GFP::TBB-2 or mCherry::tubulin.	(3) DM1A-AF488 conjugate. (4) mNG::ZYG-8 and mCherry:tubulin.

		(2) Microtubule plus-ends : EBP-2::mKate2	(5) GFP::TBB-2
Objective	100x/1.45 NA Oil plan-Apo	100x/1.4 NA Oil HCX Plan Apo	63x/1.4 NA Oil Apochromat DIC M27
Acquisition plane(s)	Spindle plane	(1) Cortex plane in contact with the glass slide (moved the focus to 12-15 µm below the spindle plane). (2) For *zyg-8(RNAi)*: spindle plane; for *zyg-8* overexp. and *zyg-8(or484ts)*: ~3 µm below spindle plane	(3) 25-30 or (4) 10-12 z-sections centred at the spindle plane; z-step: (3) 0.17 µm, (4) 0.3 µm. (5) single spindle plane.
Camera	Andor iXon3 EMCCD 512x512	ultra-sensitive Roper Evolve EMCCD	Airyscan detector
Illumination, excitation and emission characteristics	Illumination: mercury lamp. NG channel: excitation: enhanced transmission (ET) 485/12 bandpass (BP) (AHF analysentechnik); beamsplitter: low pass (LP) 495; emission: 525/50 ET Bandpass mCherry channel: excitation: BP 530-585; beamsplitter: 600; emission: low pass 615	Illumination: Argon laser mCherry channel: laser selecting the line at 561 nm with DAPI-GFP-mCherry-Cy5 emission filter and a Quad Dichroic filter. GFP channel: laser selecting the line at 488 nm with GFP/FITC 4 nm BP excitation filter and retrieving fluorescence with a Quad Dichroic emission filter	Illumination: laser diodes (3) excitation wavelength 488 nm; main beam splitter (MBS) 488/639 and 405. (4) excitation wavelength 488 nm or 561 nm; MBS 488/561 and 405; secondary beam splitter LP525 (for 488 nm laser) or SP550 (for 561 nm laser). (5) excitation wavelength 488 nm; MBS BP 420-480 + BP 495.
Spatial resolution (µm/pixel)	0.16	0.14	(3) & (4): 0.04. (5): 0.09
Temporal resolution (frame/s)	32.498	(1) 10 (2) 2.5	(3) 41.6 s for 1 z-section. (4) 1 min 23 s for 1 z-section. (5) 944 ms per frame.
Additional parameters or equipment	Extra anti-heat and ultraviolet filters added to the mercury lamp light path for long-term time-lapse	Adaptive Focus Control (AFC, Leica)	Mode: (3) & (4): Super Resolution; (5): Confocal. Frame scanning, Bidirectional scanning. Averaging: (3) & (5) number: 2, mode: line, method: mean; (4) none.
Post-processing	None	None	Deconvolution
Software	Andor Solis (Oxford instruments)	Imaging Solution (Inscoper, SAS)	ZEN blue (Zeiss)

M5- Localisation of ZYG-8 in the C. elegans one-cell embryo

To study ZYG-8 localisation in the zygote, we used *C. elegans* strains displaying a fluorescent labelling of the microtubules (mCherry::tubulin) and a fluorescent labelling of ZYG-8 (mNG::ZYG-8). We analysed deconvolved dual-colour images of fixed embryos obtained by the Airyscan 2 microscope. We investigated pixel-wise colocalisation by producing a scatterplot (Figure S1G-H). We quantified the colocalisation by computing Pearson's correlation coefficient, *r*, and performed the Costes statistical test to evaluate the significance of *r* using 200 rounds of randomisation and a bin width of 0.001 (Costes et al., 2004). This analysis was performed using Fiji and the JACoP plugin (Bolte and Cordelières, 2006).

M6- Quantification of zyg-8 under- and over-expressions at the worm and embryo levels

To quantify the ZYG-8 level at the worm level, we performed a Western blot analysis using protein extracts obtained from different *C. elegans* strains (Figure S2A-B). For each experiment, 30 adult hermaphrodites were picked into 200 µL of M9 buffer and snap-frozen in liquid nitrogen, then thawed, mixed with 6.5 µL loading buffer (DTT 0.1 M), and loaded onto a Mini Protean TGX 4–20% Tris-Glicine gel from Bio-Rad (Hercules, CA). Immunoblots were probed using the primary anti-OLLAS antibody (Novus Biologicals NBP1-06713, 1 mg/mL, host: rat) diluted at 1/2000 and the primary anti-tubulin antibody (Sigma-Aldrich T5168, host: mouse) diluted at 1/2000, and then revealed using an HRP (horseradish peroxidase) conjugated secondary antibody (1:20000; Jackson ImmunoResearch, West Grove, PA; host: rat for antiOLLAS & mouse for anti-tubulin). Membrane saturation and all antibody dilutions were made in PBS–Tween 0.2% and 5% non-fat dry milk. Blots were incubated with WesternBright ECL spray (Advansta K-12049-D50) before detecting by chemiluminescence on an Amersham Imager 680 (GeHealthcare, Chicago, IL). Quantification was performed using Fiji (Schindelin et al., 2012).

To complement the first quantification, we analysed deconvolved dual-colour images of embryos carrying two fluorescent tags: mCherry::tubulin and mNG::ZYG-8. For each embryo, we realised, in the same regions of interest (ROI), red and green fluorescence intensity measurements (mean within ROI) using Fiji: 2 square ROIs (40 x 40 pixels; 1.6 x 1.6 µm) within the spindle (1 per half-spindle), 3 square ROIs (40 x 40 pixels) within the cytoplasm, 5 curvilinear ROIs on astral microtubules using the segmented line tool, and a ROI (40 x 40 pixels) outside the embryo, the latter to measure the background fluorescence. For spindle and cytoplasm measurements, fluorescence quantification was performed on maximum projected images (3 z-sections centred on the spindle mid-plane). After subtracting the background fluorescence (ROI mean intensity) to each fluorescence of interest (spindle, cytoplasm and astral microtubule) and for each channel separately, we computed the ratio of ZYG-8 fluorescence over tubulin fluorescence for the three measurements (Figure S2C-D).

M7- Mapping astral microtubules and characterising their local curvatures and their tortuosity

We stained microtubules using an anti-α-Tubulin antibody, clone DM1A raised in mouse, Alexa Fluor® 488 conjugate (Sigma-Aldrich 16-232), diluted at 1/500 in PBS-Tween (0.2%) with BSA (1%). It targets several α-tubulin isoforms in various species. Antibody incubation was performed overnight at 4°C. Slides were then rinsed for 10 minutes in PBS-Tween (0.2%), twice, in a light-free environment. We could then visualise microtubules all along their length.

We identified the z-section(s) as the more appropriate for astral microtubule segmentation. For most embryos, we found a single z-section per embryo for which both centrosome asters were visible. For some embryos having the two centrosomes on distinct z-sections, we considered two planes of interest. We ensured that these two planes were at least 1 µm apart to consider them as two different populations of astral microtubules.

Five-step image processing pipeline to map the local curvatures of the astral microtubules (Figure S3A). **(1)** We used the planes above and below the plane of interest to perform an extended depth of field projecting the 3 z-sections into a single image (Figure S3B) (Forster et al., 2004). We thus better visualise microtubules all along their length. **(2)** We applied the *Orientation Filter Transform* (OFT, number of orientations = 20; radius = 5 pixels) since it is effective in enhancing filamentous structures against noises (Figure S3C) (Sandberg and Brega, 2007; Zhang et al., 2017). **(3)** We then used the interactive machine-learning tool, *Ilastik,* to segment the astral microtubules (Figure S3D). The dedicated paragraph below provides more detailed information about our segmentation. **(4)** We generated the skeleton of the filament traces from the binary segmentation, taking advantage of *SOAX* (Figure S3E). Further information about the use of SOAX is available in a dedicated paragraph below. **(5)** We finally measured the local curvatures of astral microtubules pixel-by-pixel from the skeleton coordinates, enabling mapping of the local curvatures (Figure S3F). Local curvatures along microtubules were computed according to the three-point method (Bicek et al., 2007) using a code retrieved on Matlab Central (Kroon, 2011). In a nutshell, microtubules are viewed as parametrised curves; at each point, the *x* and *y* coordinates are represented as second-order polynomials of the curvilinear abscissa passing through the point and its two neighbours. The curvature is then computed with the Frenet-Serret formula.

Ilastik: We initially trained *Ilastik* using the conditions *zyg-8(RNAi)* and its control during metaphase. This involved approximately 10 manual annotations of microtubules across 3 embryos for each condition to cover various intensities, contrasts and microtubule shapes. We then used this trained model, referred to as #1M (M for metaphase), to segment, in a semi-supervised way, the astral microtubules in metaphase images. Next, we trained the model to segment anaphase images of *zyg-8(RNAi)* treated embryos and their controls. Indeed, denser microtubule networks in anaphase required additional annotations. This led to the upgraded model #1A that we used to segment anaphase images. We then analysed *zyg-8(or484ts)* mutants and untreated embryos in metaphase. The model was further improved by manually annotating 3 mutants, resulting in model #2M, which we used to segment images of both mutants and untreated embryos in metaphase. We applied a similar process for segmenting anaphase images of mutants and untreated embryos, enhancing model #2M with a few annotations of anaphase mutants to get the model #2A. The table below summarised the *Ilastik* models used to produce the data displayed in the different figures.

***Ilastik* model**	**Used for data displayed in figures**
#1M	2A; 2E & 3B (*zyg-8(RNAi)* and control); S4 (only metaphase)
#1A	2B; 2F & 3C (*zyg-8(RNAi)* and control); S4 (only anaphase)
#2M	2C; 2E & 3B (*zyg-8(or484ts)* and untreated); S5 (only metaphase)
#2A	2D; 2F & 3C (*zyg-8(or484ts)* and untreated); S5 (only anaphase)

SOAX: We extracted the centrelines from the thick filaments utilising SOAX mostly with standard parameters, making a few specific adjustments, which are highlighted in the table

below. These five parameters were crucial for accurately delineating the curved regions of the microtubules. The settings used ensured that the centrelines faithfully represented the shapes of the microtubules, as confirmed through visual validation. Additionally, manual corrections could be applied at this stage, such as when two microtubules were mistakenly merged into one.

***SOAX* parameter name**	**Parameter value**
Snake Point Spacing	4
Beta	0.01
Stretch Factor (k_str)	0.8
Radial Near (pixels)	8
Radial Far (pixels)	16

Microtubule shape quantification: We conducted three complementary analyses only from segmented astral microtubules that were at least 4 µm long, as shorter ones often represented fragments. This approach was appropriate for comparing conditions without seeking absolute quantification.

(1) For each z-projected section, we calculated the normalised histogram of local curvatures (Figure S3G) and averaged these histograms per condition (e.g., Figure 2A, red).

(2) We determined the 95th percentile curvature for each microtubule to capture faithfully the highest curvatures and then computed the median of the values over the microtubules of each z-projected section. We finally compared the set of medians of each condition (e.g., Figure 2E).

(3) We measured the tortuosity for each microtubule, defined as the curvilinear distance divided by the end-to-end distance (Figure 3A). Straight microtubules have tortuosity values near one, while bent microtubules show higher values. Then, we calculated the medians of tortuosity for each z-projected section and compared the set of medians of each condition (e.g., Figure 3B).

M8- Simulation using Cytosim

We used *Cytosim* to simulate cytoskeletal filaments (Nedelec and Foethke, 2007). We modified *Cytosim* to allow multiple fibre types to emanate from a single aster and to exert a given external force on solids, fibres or spheres (doi: 10.5281/zenodo.14246919). We conducted a 2D simulation of the first mitosis of the *C. elegans* zygote, focusing on spindle positioning and the astral microtubule network (Figure S6A). The simulation represented the spindle as a rigid rod implemented with static spindle microtubules, excluding any dynamic elements such as motor proteins. The parameters used in the simulation are detailed in Table S2. Importantly, to mimic cortical asymmetric pulling forces, we applied external forces at the spindle poles: -180 pN at the anterior pole and +300 pN at the posterior pole (Grill et al., 2003). We attached two types of fibres to each solid, which simulated the centrosomes, to differentiate between spindle and astral microtubules. The astral microtubules were defined as fibres without dynamics at their minus ends and with plus-ends displaying classic dynamic instability. We set their total number to 75, according to our estimated count of astral microtubules longer than about 2 µm in a 2D plane. Their rigidities were varied at 2, 10, or 25 pN·µm², reflecting the range of *in vitro* measurements (Hawkins et al., 2010), with these differences allowing for visible variations in microtubule curvatures. Additionally, these fibres could engage with cortical force generators simulated as hands bound to the cortex.

We measured both the highest curvatures (95th percentile) and the tortuosity of the astral microtubules (Figure S6B-C) after 45 seconds of simulation, following the approach outlined in method M7.
To estimate the durations of fibre cortical contacts, we analysed fibre lengths, end positions, and cortical anchor positions. When microtubules push against the cortex, they grow slowly due to the force-velocity relationship, remaining near the cell cortex. We first tracked fibre lengths over time to identify instances of very low growth rates (under 0.18 µm/s), indicating moments when the fibres were stalled (neither growing nor shrinking). Next, we calculated the distances between fibre end positions and cortical anchor (hand) positions during these stalling events to identify the events whose distance was below 1 µm. Over 45 seconds (beginning 15 seconds after the simulation started to allow for warm-up), we recorded the durations of fibre cortical contacts and constructed the corresponding histogram. We then fitted it with a mono-exponential model (Kozlowski et al., 2007; Sugioka et al., 2018). This analysis yielded a characteristic lifetime for each simulation run (Figure S6D).

M9- Landing assay to study astral microtubule cortical contacts

The entire microtubule lattices were fluorescently labelled using GFP::TBB-2 or mCherry::tubulin to view them in all their states. We used the same approach as the one previously implemented in (Bouvrais et al., 2021) and available on Zenodo (doi: 10.5281/zenodo.4552485); we combined a Kalman filtering (gain set to 0.5 and initial noise to 0.05) and *u-track* whose parameters are listed in the table below. After tracking the microtubule contacts, we could compute the duration histograms of astral microtubule contacts per embryo and averaged them among each condition (e.g., Figure 4A). We then performed the DiLiPop analysis to read the characteristic lifetimes and densities of the cortical pulling and pushing events (e.g., Figure 5CD). The latter densities of events are distinct from instantaneous contact density and were thus independent of the cortical contact durations (Bouvrais et al., 2021).

u-track step	**Parameter name**	**Parameter value**
Detection	Gaussian standard deviation	1.2
	Alpha-value for initial detection of local maxima	0.14* / 0.12**
	Rolling window time-averaging	3
	Iterative Gaussian mixture-model fitting	0
Tracking	Maximum gap to close	5
	Merge split	0
	Minimum length of track segments from the first step	1
Cost function frame-to-frame linking	Flag for linear motion	1
	Allow instantaneous direction reversal	1
	Search radius lower limit	1
	Search radius upper limit	3
	Standard deviation multiplication factor	3
	Nearest neighbour distance calculation	1
	Number of frames for nearest neighbour distance calculation	4
Cost function close gaps	Flag for linear motion	1
	Search radius lower limit	1
	Search radius upper limit	3
	Standard deviation multiplication factor	3

Nearest neighbour distance calculation	Number of frames for nearest neighbour	4
	Penalty for increasing gap length	1.5
	Maximum angle between linear tracks segments	30

* for GFP::TBB-2 labelling; ** for mCherry::tubulin labelling.

M10- Characterisation of astral microtubule growing and nucleation rates

We labelled microtubule plus-ends using EBP-2::mKate2 and performed an analysis adapted from (Srayko et al., 2005) using Fiji (except otherwise cited). We measured microtubule dynamics during metaphase.

To measure the growth rates, we first denoised the movies using Kalman filtering, with the gain set to 0.5 and the initial noise estimate set to 0.05. Next, we traced a line along the comet trajectory in the pre-processed movie, focussing on comets that remained visible for at least 10 frames (4 s). We generated a kymograph from the traced line to assess comet displacement velocity. We repeated the measurement approximately 50 times for each condition across about ten embryos (about 25 comets per centrosome).

To measure the nucleation rate, we first denoised the movies using Candle filtering (parameters: *beta* = 0.1; *patchRadius* = 1; *searchRadius* = 3; *back* = 1). We did not apply additional pre-processing for *zyg-8(RNAi)* treatment, *zyg-8* overexpression and their control. However, for *zyg-8(or484ts)* mutants and untreated embryos, we enhanced contrast using an unsharp mask (*radius* = 1; *Mask weight* = 0.7). Since centrosomes moved during metaphase, we applied Icy's rigid registration plugin (v1.4) on the denoised images (de Chaumont et al., 2012). This registration aligns each image with a reference image to correct for centrosome displacements, as described in (Soler et al., 2022). Doing so, we accurately counted the comets crossing a half-circle region of interest (ROI) positioned 9 µm from the centrosome after (Srayko et al., 2005). We generated kymographs over 150 frames (60 seconds). To address the inhomogeneous background in the raw kymographs, we applied background subtraction using Gaussian blurring. We then set an intensity threshold to retain the brightest 2% of pixels in *zyg-8(RNAi)* and control kymographs, and 2.5% for *zyg-8* overexpression ones, *zyg-8(or484ts)*, and their controls. Finally, we used the "Analyze particles" command and counted objects considered as individual EBP-2 comets (particle size: 2 pixels to infinity, 0.14 µm/pixel). Measurements were done for both anterior and posterior centrosomes, except when reduced quality of the imaging plane allowed for accurate characterisation of a single centrosome.

M11- Centrosome-tracking assay and oscillation characterisation

The tracking of labelled centrosomes (e.g., mCherry::TBG-1) and the analysis of their trajectories were conducted using custom tracking software developed using Matlab (The MathWorks) (Pécréaux et al., 2006a). Tracking of γ-tubulin labelled embryos fixed in -20°C methanol demonstrated an accuracy of 10 nm (Pécréaux et al., 2016). To determine embryo orientations and centres, we performed cross-correlation of the embryo background cytoplasmic fluorescence with artificial binary images that represented an embryo. We calculated the embryo size (lengths of the long and short axes) using the active contour algorithm (Pécréaux et al., 2006b). From the spindle pole positions, we measured the maximal amplitudes of anaphase oscillations (peak-to-peak) for both poles, normalised by the short axis of the embryo, as well as their maximum frequencies (e.g., Figure 5A-B). We also assessed the most posterior positions of the posterior centrosome, normalised by the embryo's long axis, since this posterior displacement reflects cortical pulling forces (e.g., Figure S9) (Pécréaux

et al., 2006a). Finally, we quantified the spindle position (the midpoint between the 2 centrosomes), and the spindle orientation (the angle between the spindle axis and the embryo's long axis) at the end of mitosis, specifically at 150 s after the anaphase onset (Figure 6C-D).

M12- Centrosome-size measurements

We analysed images of embryos labelled with mCherry::TBG-1 or GFP::TBG-1 by tracking their centrosomes (cf. M11). From the tracked positions, we extracted vignettes of 6.4 x 6.4 µm (40 x 40 pixels). We then performed a 2D Gaussian least-square fit to characterise both the posterior and anterior centrosomes every second, using code from (Kolin, 2003)). From these fits, we obtained the *x*- and *y*-widths and calculated the diameter of the centrosomes, assuming they are round, using the formula: $D = \sqrt{x^2 + y^2}$.

M13- Fourier analysis of the positional micromovements

We investigated the micromovements of spindle position along the transverse axis over time, based on our previously published method (Pecreaux et al., 2016). From the time series of the spindle position along the transverse axis during anaphase obtained by tracking the poles (cf. M11), we computed the power spectral density (*PSD*) of the signal multiplied by the Hann window to safeguard against artefact due to the position difference between the beginning and end of the considered time interval (Mercat, 2016). It contrasted with (Pécréaux et al., 2016), where we selected only embryos with low drift in their position over time, rather than windowing. The Hann windows appeared a sensible choice to fit the *PSD* later since its discrete Fourier transform has only 3 non-zeros coefficients (harris, 1978; Mercat, 2016); therefore, once convolved to the real *PSD* of the spindle length, it minimally "blur" it.

We then fitted this *PSD* with a second-order Lorentzian model, as in (Pécréaux et al., 2016). Along a mechanistic line, this model corresponds to a Kelvin-Voigt-with-inertia discrete model corresponding to a Hookean spring (centring, *K*), a dashpot (damping, *G*), and an inertial element (*I*) in parallel. However, these quantities, when retrieved by fitting, depend on the amplitude of the stochastic noise that powers the fluctuations. We, therefore, utilised an alternative representation featuring (1) a diffusion coefficient *D*, inversely proportional to the damping *G* and dependent on the stochastic noise, (2) the centring-to-damping corner frequency f_c ($\propto K/G$) reflecting centring efficiency, and (3) the damping-to-inertia corner frequency f_0 ($\propto G/I$); the inertia *I* arising from load-dependent detachment of force generators as for anaphase rocking (Pécréaux et al., 2006a). Such a model was transformed into the Fourier space and convolved on the fly with the transform of the Hann window to perform the fit (Mercat, 2016). We then performed the fit using augmented Lagrangians and refined it using the pattern search algorithm (Audet and Dennis Jr, 2002; Pierre and Lowe, 1975) as implemented in (Mercat, 2016).

M14- Statistics

Difference between two samples was assessed by the two-tailed Student's *t*-test with Welch–Satterthwaite correction for unequal variance. When Gaussian distribution cannot be assumed, we used the Mann–Whitney test (also called the Wilcoxon rank-sum test). We used it for instance to compare proportions of microtubule curvatures () or microtubule highest curvatures (Figure 2E-F) or microtubule tortuosity (Figure 3B-C). For the sake of simplicity, we

recorded confidence levels using diamond (◊, $0.01 < p \leq 0.05$), stars (*, $0.001 < p \leq 0.01$; **, $1x10^{-4} < p \leq 0.001$; ***, $1x10^{-5} < p \leq 1x10^{-4}$) or ns (non-significant, $p > 0.05$). We abbreviated the standard deviation by SD. Last, we used the Kolmogorov–Smirnov test to reveal whether the two distributions differed significantly (distributions of contact durations or of local curvatures).

Acknowledgements

Some strains were provided by the Caenorhabditis Genetics Center (CGC), which is funded by National Institutes of Health Office of Research Infrastructure Programs (P40 OD010440; University of Minnesota). Strains TH27 and TH430 were kindly offered by Prof Anthony A. Hyman. We thank Dr Gregoire Michaux for the feeding clone library and technical support. The CRISPR strains MCP347, MCP361 & MCP554 were generated by SeGiCel facility (CNRS UMS3453 - INSERM US7). We thank S. Dutertre and X. Pinson of the Microscopy Rennes Imaging Center (MRic, BIOSIT, Biogenouest) for assistance. MRic is member of the national infrastructure France-BioImaging supported by the French National Research Agency (ANR-10-INBS-04). In particular, we acknowledge the funding of the Zeiss Airyscan confocal microscope by EU funding FEDER under reference CARE Phase 2 and the Zeiss Airyscan 2 confocal microscope by INCA, Rennes Métropole, CPER and Biosit. Spinning disc microscope was co-funded by the CNRS, Rennes Metropole (AIS 16C0400) and Region Bretagne (AniDyn-MTgrant). L.C. was supported by a PhD fellowship from “La Ligue Nationale Contre le Cancer” (2021-2024). H.B. was supported by ANR grant (MICENN), “La Ligue Régionale Contre le Cancer » (Ille-et-Vilaine & Deux-Sèvres committees in 2019 ; Côtes d’Armor & Ille-et-Vilaine committees in 2021), University of Rennes (Défis scientifiques, 2019). We thank the Pécréaux lab for their support, the Gibeaux, Giet, Huet, Michaux, and Tramier labs for helpful discussions, L. Chesneau for his assistance in designing the CRISPR strains, and A. Pacquelet and C. Heligon for their careful reading of the manuscript.

Author contributions

Conceptualisation: HB, JP; Experimental data: LC, SP, EH, MC, TS, HB; Data curation: HB; Formal analysis: LC, EH, MC, JP, HB; Funding acquisition: JP, HB; Methodology: LC, JP, HB; Project administration: HB; Software: JP, HB; Supervision: JP, HB; Validation: LC, EH, JP, HB; Visualisation: LC, HB; Writing – original draft: HB; Writing – review and editing: LC, JP, HB.

REFERENCES

Akhmanova, A., and L.C. Kapitein. 2022. Mechanisms of microtubule organization in differentiated animal cells. *Nature Reviews Molecular Cell Biology*. 23:541-558.

Arjona, M.I., J. Najafi, and N. Minc. 2023. Cytoplasm mechanics and cellular organization. *Current Opinion in Cell Biology*. 85:102278.

Audet, C., and J.E. Dennis Jr. 2002. Analysis of generalized pattern searches. *SIAM Journal on optimization*. 13:889-903.

Baena-López, L.A., A. Baonza, and A. García-Bellido. 2005. The Orientation of Cell Divisions Determines the Shape of Drosophila Organs. *Current Biology*. 15:1640-1644.

Balabanian, L., C.L. Berger, and A.G. Hendricks. 2017. Acetylated Microtubules Are Preferentially Bundled Leading to Enhanced Kinesin-1 Motility. *Biophysical journal*. 113:1551-1560.

Baumgart, J., M. Kirchner, S. Redemann, J. Woodruff, J.-M. Verbavatz, F. Julicher, A. Hyman, T. Mueller-Reichert, and J. Brugues. 2019. Soluble tubulin is locally enriched at mitotic centrosomes in C. elegans. *bioRxiv*:543066.

Bechstedt, S., and G.J. Brouhard. 2012. Doublecortin recognizes the 13-protofilament microtubule cooperatively and tracks microtubule ends. *Developmental Cell*. 23:181-192.

Bellanger, J.-M., J.C. Carter, J.B. Phillips, C. Canard, B. Bowerman, and P. Gönczy. 2007. ZYG-9, TAC-1 and ZYG-8 together ensure correct microtubule function throughout the cell cycle of C. elegans embryos. *Journal of Cell Science*. 120:2963-2973.

Bellanger, J.-M., J.G. Cueva, R. Baran, G. Tang, M.B. Goodman, and A. Debant. 2012. The doublecortin-related gene zyg-8 is a microtubule organizer in Caenorhabditis elegans neurons. *Journal of Cell Science*. 125:5417-5427.

Bergstralh, D.T., N.S. Dawney, and D. St Johnston. 2017. Spindle orientation: a question of complex positioning. *Development*. 144:1137-1145.

Bicek, A.D., E. Tüzel, A. Demtchouk, M. Uppalapati, W.O. Hancock, D.M. Kroll, and D.J. Odde. 2009. Anterograde Microtubule Transport Drives Microtubule Bending in LLC-PK1 Epithelial Cells. *Molecular biology of the cell*. 20:2943-2953.

Bicek, A.D., E. Tüzel, D.M. Kroll, and D.J. Odde. 2007. Analysis of Microtubule Curvature. *In* Methods in Cell Biology. Vol. 83. Academic Press. 237-268.

Bielas, S.L., F.F. Serneo, M. Chechlacz, T.J. Deerinck, G.A. Perkins, Patrick B. Allen, M.H. Ellisman, and J.G. Gleeson. 2007. Spinophilin Facilitates Dephosphorylation of Doublecortin by PP1 to Mediate Microtubule Bundling at the Axonal Wrist. *Cell*. 129:579-591.

Blob, A., D. Ventzke, G. Nies, J.N. Dühmert, B. Schmitzer, A. Munk, L. Schaedel, and S. Köster. 2023. Vimentin intermediate filaments structure and mechanically support microtubules in cells. *bioRxiv*:2023.2004.2019.537509.

Bolte, S., and F.P. Cordelières. 2006. A guided tour into subcellular colocalization analysis in light microscopy. *Journal of Microscopy*. 224:213-232.

Bougé, A.-L., and M.-L. Parmentier. 2016. Tau excess impairs mitosis and kinesin-5 function, leading to aneuploidy and cell death. *Disease Models & Mechanisms*. 9:307-319.

Bouvrais, H., L. Chesneau, Y. Le Cunff, D. Fairbrass, N. Soler, S. Pastezeur, T. Pécot, C. Kervrann, and J. Pécréaux. 2021. The coordination of spindle-positioning forces during the asymmetric division of the Caenorhabditis elegans zygote. *EMBO reports*. 22:e50770.

Bouvrais, H., L. Chesneau, S. Pastezeur, D. Fairbrass, M. Delattre, and J. Pécréaux. 2018. Microtubule Feedback and LET-99-Dependent Control of Pulling Forces Ensure Robust Spindle Position. *Biophysical journal*. 115:2189-2205.

Brangwynne, C.P., F.C. MacKintosh, S. Kumar, N.A. Geisse, J. Talbot, L. Mahadevan, K.K. Parker, D.E. Ingber, and D.A. Weitz. 2006. Microtubules can bear enhanced compressive loads in living cells because of lateral reinforcement. *The Journal of cell biology*. 173:733-741.

Brenner, S. 1974. The genetics of Caenorhabditis elegans. *Genetics*. 77:71-94.

Brun, L., B. Rupp, J.J. Ward, and F. Nédélec. 2009. A theory of microtubule catastrophes and their regulation. *Proceedings of the National Academy of Sciences*. 106:21173-21178.

Bunker, J.M., L. Wilson, M.A. Jordan, and S.C. Feinstein. 2004. Modulation of microtubule dynamics by tau in living cells: implications for development and neurodegeneration. *Molecular biology of the cell*. 15:2720-2728.

Burute, M., and L.C. Kapitein. 2019. Cellular Logistics: Unraveling the Interplay Between Microtubule Organization and Intracellular Transport. *Annual Review of Cell and Developmental Biology*. 35:29-54.

Chaaban, S., S. Jariwala, C.-T. Hsu, S. Redemann, J.M. Kollman, T. Müller-Reichert, D. Sept, K.H. Bui, and G.J. Brouhard. 2018. The Structure and Dynamics of C. elegans Tubulin Reveals the Mechanistic Basis of Microtubule Growth. *Developmental Cell*.

Chawla, D.G., R.V. Shah, Z.K. Barth, J.D. Lee, K.E. Badecker, A. Naik, M.M. Brewster, T.P. Salmon, and N. Peel. 2016. Caenorhabditis elegans glutamylating enzymes function redundantly in male mating. *Biology Open*. 5:1290-1298.

Chrétien, D., F. Metoz, F. Verde, E. Karsenti, and R.H. Wade. 1992. Lattice defects in microtubules: protofilament numbers vary within individual microtubules. *The Journal of cell biology*. 117:1031-1040.

Costes, S.V., D. Daelemans, E.H. Cho, Z. Dobbin, G. Pavlakis, and S. Lockett. 2004. Automatic and quantitative measurement of protein-protein colocalization in live cells. *Biophysical journal*. 86:3993-4003.

Couillard-Despres, S., G. Uyanik, S. Ploetz, C. Karl, H. Koch, J. Winkler, and L. Aigner. 2004. Mitotic impairment by doublecortin is diminished by doublecortin mutations found in patients. *Neurogenetics*. 5:83-93.

Czajkowski, E.R., Y. Zou, N.S. Divekar, and S.M. Wignall. 2024. The doublecortin-family kinase ZYG-8DCLK1 regulates microtubule dynamics and motor-driven forces to promote the stability of C. elegans acentrosomal spindles. *PLOS Genetics*. 20:e1011373.

de Chaumont, F., S. Dallongeville, N. Chenouard, N. Hervé, S. Pop, T. Provoost, V. Meas-Yedid, P. Pankajakshan, T. Lecomte, Y. Le Montagner, T. Lagache, A. Dufour, and J.-C. Olivo-Marin. 2012. Icy: an open bioimage informatics platform for extended reproducible research. *Nature methods*. 9:690.

Decker, M., S. Jaensch, A. Pozniakovsky, A. Zinke, Kevin F. O'Connell, W. Zachariae, E. Myers, and Anthony A. Hyman. 2011. Limiting Amounts of Centrosome Material Set Centrosome Size in C. elegans Embryos. *Current Biology*. 21:1259-1267.

Dema, A., R.A. Charafeddine, J.v. Haren, S. Rahgozar, G. Viola, K.A. Jacobs, M.L. Kutys, and T. Wittmann. 2024. Doublecortin reinforces microtubules to promote growth cone advance in soft environments. *bioRxiv*:2024.2002.2028.582626.

di Pietro, F., A. Echard, and X. Morin. 2016. Regulation of mitotic spindle orientation: an integrated view. *EMBO reports*.

Dogterom, M., J.W.J. Kerssemakers, G. Romet-Lemonne, and M.E. Janson. 2005. Force generation by dynamic microtubules. *Current Opinion in Cell Biology*. 17:67-74.

Duerr, J.S. 2013. Antibody staining in C. elegans using "freeze-cracking". *J Vis Exp*.

Ettinger, A., J. van Haren, Susana A. Ribeiro, and T. Wittmann. 2016. Doublecortin Is Excluded from Growing Microtubule Ends and Recognizes the GDP-Microtubule Lattice. *Current Biology*. 26:1549-1555.

Farhadifar, R., C.-H. Yu, G. Fabig, H.-Y. Wu, D.B. Stein, M. Rockman, T. Müller-Reichert, M.J. Shelley, and D.J. Needleman. 2020. Stoichiometric interactions explain spindle dynamics and scaling across 100 million years of nematode evolution. *Elife*. 9:e55877.

Fededa, J.P., C. Esk, B. Mierzwa, R. Stanyte, S. Yuan, H. Zheng, K. Ebnet, W. Yan, J.A. Knoblich, and D.W. Gerlich. 2016. MicroRNA‐34/449 controls mitotic spindle orientation during mammalian cortex development. *The EMBO Journal*. 35:2386-2398.

Felgner, H., R. Frank, J. Biernat, E.-M. Mandelkow, E. Mandelkow, B. Ludin, A. Matus, and M. Schliwa. 1997. Domains of neuronal microtubule-associated proteins and flexural rigidity of microtubules. *The Journal of cell biology*. 138:1067-1075.

Felgner, H., R. Frank, and M. Schliwa. 1996. Flexural rigidity of microtubules measured with the use of optical tweezers. *Journal of Cell Science*. 109:509-516.

Fielmich, L.-E., R. Schmidt, D.J. Dickinson, B. Goldstein, A. Akhmanova, and S. Van den Heuvel. 2018. Optogenetic dissection of mitotic spindle positioning in vivo. *Elife*. 7:e38198.

Fischer, E., E. Legue, A. Doyen, F. Nato, J.-F. Nicolas, V. Torres, M. Yaniv, and M. Pontoglio. 2006. Defective planar cell polarity in polycystic kidney disease. *Nature Genetics*. 38:21-23.

Fleming, E.S., M. Temchin, Q. Wu, L. Maggio-Price, and J.S. Tirnauer. 2009. Spindle misorientation in tumors from APC mice. *Molecular Carcinogenesis*. 48:592-598.

Forster, B., D. Van De Ville, J. Berent, D. Sage, and M. Unser. 2004. Extended depth-of-focus for multi-channel microscopy images: a complex wavelet approach. *In* Biomedical Imaging: Nano to Macro, 2004. IEEE International Symposium on. IEEE. 660-663.

Forth, S., and T.M. Kapoor. 2017. The mechanics of microtubule networks in cell division. *J Cell Biol*. 216:1525-1531.

Fourniol, F.J., C.V. Sindelar, B. Amigues, D.K. Clare, G. Thomas, M. Perderiset, F. Francis, A. Houdusse, and C.A. Moores. 2010. Template-free 13-protofilament microtubule–MAP assembly visualized at 8 Å resolution. *The Journal of Cell Biology*. 191:463-470.

Gao, L., Z. Yang, C. Hiremath, S.E. Zimmerman, B. Long, P.R. Brakeman, K.E. Mostov, D.M. Bryant, K. Luby-Phelps, and D.K. Marciano. 2017. Afadin orients cell division to position the tubule lumen in developing renal tubules. *Development*. 144:3511-3520.

Gao, T., M. Wang, L. Xu, T. Wen, J. Liu, and G. An. 2016. DCLK1 is up-regulated and associated with metastasis and prognosis in colorectal cancer. *J Cancer Res Clin Oncol*. 142:2131-2140.

Garcin, C., and A. Straube. 2019. Microtubules in cell migration. *Essays in Biochemistry*. 63:509-520.

Gargini, R., B. Segura-Collar, and P. Sánchez-Gómez. 2019. Novel Functions of the Neurodegenerative-Related Gene Tau in Cancer. *Frontiers in Aging Neuroscience*. 11.

Garzon-Coral, C., H.A. Fantana, and J. Howard. 2016. A force-generating machinery maintains the spindle at the cell center during mitosis. *Science*. 352:1124-1127.

Ge, Y., N. Weygant, D. Qu, R. May, W.L. Berry, J. Yao, P. Chandrakesan, W. Zheng, L. Zhao, K.L. Zhao, M. Drake, K.J. Vega, M.S. Bronze, J.J. Tomasek, G. An, and C.W. Houchen. 2018. Alternative splice variants of DCLK1 mark cancer stem cells, promote self-renewal and

drug-resistance, and can be targeted to inhibit tumorigenesis in kidney cancer. *Int J Cancer*. 143:1162-1175.

Gittes, F., B. Mickey, J. Nettleton, and J. Howard. 1993. Flexural rigidity of microtubules and actin filaments measured from thermal fluctuations in shape. *The Journal of cell biology*. 120:923-934.

Goedert, M., C. Baur, J. Ahringer, R. Jakes, M. Hasegawa, M. Spillantini, M. Smith, and F. Hill. 1996. PTL-1, a microtubule-associated protein with tau-like repeats from the nematode Caenorhabditis elegans. *Journal of cell science*. 109:2661-2672.

Gönczy, P., J.M. Bellanger, M. Kirkham, A. Pozniakowski, K. Baumer, J.B. Phillips, and A.A. Hyman. 2001. zyg-8, a gene required for spindle positioning in C. elegans, encodes a doublecortin-related kinase that promotes microtubule assembly. *Developmental cell*. 1:363.

Goodson, H.V., and E.M. Jonasson. 2018. Microtubules and microtubule-associated proteins. *Cold Spring Harbor perspectives in biology*. 10:a022608.

Grill, S.W., P. GoÈnczy, E.H.K. Stelzer, and A.A. Hyman. 2001. Polarity controls forces governing asymmetric spindle positioning in theCaenorhabditis elegansembryo.

Grill, S.W., J. Howard, E. Schaffer, E.H.K. Stelzer, and A.A. Hyman. 2003. The distribution of active force generators controls mitotic spindle position. *Science*. 301:518.

Grill, S.W., and A.A. Hyman. 2005. Spindle positioning by cortical pulling forces. *Developmental Cell*. 8:461-465.

Grill, S.W., K. Kruse, and F. Jülicher. 2005. Theory of Mitotic Spindle Oscillations. *Physical Review Letters*. 94:108104.

Gudimchuk, N.B., and J.R. McIntosh. 2021. Regulation of microtubule dynamics, mechanics and function through the growing tip. *Nature Reviews Molecular Cell Biology*. 22:777-795.

Hahn, I., A. Voelzmann, J. Parkin, J. Fuelle, P.G. Slater, L.A. Lowery, N. Sanchez-Soriano, and A. Prokop. 2021. Tau, XMAP215/Msps and Eb1 co-operate interdependently to regulate microtubule polymerisation and bundle formation in axons. *bioRxiv*:2020.2008.2019.257808.

harris, f. 1978. On the Use of Windows for Harmonic Analysis With the Discrete Fourier Transform. *Proceedings of the IEEE*. 66:51-83.

Hawkins, T., M. Mirigian, M.S. Yasar, and J.L. Ross. 2010. Mechanics of microtubules. *Journal of biomechanics*. 43:23-30.

Horesh, D., T. Sapir, F. Francis, S.G. Wolf, M. Caspi, M. Elbaum, J. Chelly, and O. Reiner. 1999. Doublecortin, a stabilizer of microtubules. *Human molecular genetics*. 8:1599-1610.

Howard, J. 2006. Elastic and damping forces generated by confined arrays of dynamic microtubules. *Physical biology*. 3:54.

Howard, J., and C. Garzon-Coral. 2017. Physical Limits on the Precision of Mitotic Spindle Positioning by Microtubule Pushing forces. *BioEssays*. 39:1700122.

Ito, H., S. Tanaka, Y. Akiyama, S. Shimada, R. Adikrisna, S. Matsumura, A. Aihara, Y. Mitsunori, D. Ban, and T. Ochiai. 2016. Dominant expression of DCLK1 in human pancreatic cancer stem cells accelerates tumor invasion and metastasis. *PLoS One*. 11:e0146564.

Izumi, Y., N. Ohta, K. Hisata, T. Raabe, and F. Matsuzaki. 2006. Drosophila Pins-binding protein Mud regulates spindle-polarity coupling and centrosome organization. *Nature cell biology*. 8:586-593.

Janson, M.E., E. Mathilde, and M. Dogterom. 2003. Dynamic instability of microtubules is regulated by force. *The Journal of cell biology*. 161:1029-1034.

Jean, D.C., P.W. Baas, and M.M. Black. 2012. A novel role for doublecortin and doublecortin-like kinase in regulating growth cone microtubules. *Human molecular genetics*. 21:5511-5527.

Jingchen, L., C. Longcan, and J. Hongyuan. 2019. Cell shape and intercellular adhesion regulate mitotic spindle orientation. *Molecular biology of the cell*. 30:2458-2468.

Kadavath, H., R.V. Hofele, J. Biernat, S. Kumar, K. Tepper, H. Urlaub, E. Mandelkow, and M. Zweckstetter. 2015. Tau stabilizes microtubules by binding at the interface between tubulin heterodimers. *Proceedings of the National Academy of Sciences*. 112:7501-7506.

Kamath, R.S., and J. Ahringer. 2003. Genome-wide RNAi screening in Caenorhabditis elegans. *Methods*. 30:313-321.

Kaplan, A., and O. Reiner. 2011. Linking cytoplasmic dynein and transport of Rab8 vesicles to the midbody during cytokinesis by the doublecortin domain-containing 5 protein. *Journal of cell science*. 124:3989-4000.

Kellogg, E.H., N.M.A. Hejab, S. Poepsel, K.H. Downing, F. DiMaio, and E. Nogales. 2018. Near-atomic model of microtubule-tau interactions. *Science*. 360:1242-1246.

Kikumoto, M., M. Kurachi, V. Tosa, and H. Tashiro. 2006. Flexural rigidity of individual microtubules measured by a buckling force with optical traps. *Biophysical journal*. 90:1687-1696.

Kim, M.H., T. Cierpicki, U. Derewenda, D. Krowarsch, Y. Feng, Y. Devedjiev, Z. Dauter, C.A. Walsh, J. Otlewski, J.H. Bushweller, and Z.S. Derewenda. 2003. The DCX-domain tandems of doublecortin and doublecortin-like kinase. *Nature Structural & Molecular Biology*. 10:324-333.

Kimura, K., and A. Kimura. 2011. Intracellular organelles mediate cytoplasmic pulling force for centrosome centration in the Caenorhabditis elegans early embryo. *Proceedings of the National Academy of Sciences*. 108:137-142.

Kolin, D. 2003. Image correlation spectroscopy.

Kotak, S. 2019. Mechanisms of Spindle Positioning: Lessons from Worms and Mammalian Cells. *Biomolecules*. 9:80.

Kozlowski, C., M. Srayko, and F. Nedelec. 2007. Cortical Microtubule Contacts Position the Spindle in C. elegans Embryos. *Cell*. 129:499-510.

Kroon, D.-J. 2011. 2D line curvature and normals. Mathworks.

Kurachi, M., M. Hoshi, and H. Tashiro. 1995. Buckling of a single microtubule by optical trapping forces: direct measurement of microtubule rigidity. *Cell motility and the cytoskeleton*. 30:221-228.

Kurz, J.C., and R.C. Williams Jr. 1995. Microtubule-associated proteins and the flexibility of microtubules. *Biochemistry*. 34:13374-13380.

Lechler, T., and M. Mapelli. 2021. Spindle positioning and its impact on vertebrate tissue architecture and cell fate. *Nature Reviews Molecular Cell Biology*. 22:691-708.

Li, S., S. Besson, C. Blackburn, M. Carroll, R.K. Ferguson, H. Flynn, K. Gillen, R. Leigh, D. Lindner, M. Linkert, W.J. Moore, B. Ramalingam, E. Rozbicki, G. Rustici, A. Tarkowska, P. Walczysko, E. Williams, C. Allan, J.-M. Burel, J. Moore, and J.R. Swedlow. 2016. Metadata management for high content screening in OMERO. *Methods*. 96:27-32.

Li, W., H.A. Crellin, D. Cheerambathur, and F.J. McNally. 2023. Redundant microtubule crosslinkers prevent meiotic spindle bending to ensure diploid offspring in C. elegans. *PLOS Genetics*. 19:e1011090.

Lin, P.T., J.G. Gleeson, J.C. Corbo, L. Flanagan, and C.A. Walsh. 2000. DCAMKL1 Encodes a Protein Kinase with Homology to Doublecortin that Regulates Microtubule Polymerization. *The Journal of Neuroscience*. 20:9152-9161.

Liu, H., T. Wen, Y. Zhou, X. Fan, T. Du, T. Gao, L. Li, J. Liu, L. Yang, and J. Yao. 2019. DCLK1 plays a metastatic-promoting role in human breast cancer cells. *BioMed Research International*. 2019.

Liu, J.S., C.R. Schubert, X. Fu, F.J. Fourniol, J.K. Jaiswal, A. Houdusse, C.M. Stultz, C.A. Moores, and C.A. Walsh. 2012. Molecular basis for specific regulation of neuronal kinesin-3 motors by doublecortin family proteins. *Molecular cell*. 47:707-721.

Maiato, H., A.M. Gomes, F. Sousa, and M. Barisic. 2017. Mechanisms of Chromosome Congression during Mitosis. *Biology*. 6:13.

Manka, Szymon W., and Carolyn A. Moores. 2018. Microtubule structure by cryo-EM: snapshots of dynamic instability. *Essays In Biochemistry*.

Manka, S.W., and C.A. Moores. 2020. Pseudo-repeats in doublecortin make distinct mechanistic contributions to microtubule regulation. *EMBO reports*. 21:e51534.

Mao, Y., A.L. Tournier, P.A. Bates, J.E. Gale, N. Tapon, and B.J. Thompson. 2011. Planar polarization of the atypical myosin Dachs orients cell divisions in Drosophila. *Genes Dev*. 25:131-136.

Matis, M. 2020. The Mechanical Role of Microtubules in Tissue Remodeling. *BioEssays*. 42:1900244.

Maurer, S.P., F.J. Fourniol, G. Bohner, C.A. Moores, and T. Surrey. 2012. EBs recognize a nucleotide-dependent structural cap at growing microtubule ends. *Cell*. 149:371-382.

McDermott, J.B., S. Aamodt, and E. Aamodt. 1996. ptl-1, a Caenorhabditis elegans gene whose products are homologous to the τ microtubule-associated proteins. *Biochemistry*. 35:9415-9423.

McNally, F.J. 2013. Mechanisms of spindle positioning. *The Journal of cell biology*. 200:131-140.

Mercat, B. 2016. Analyse temps-fréquence en mécanique cellulaire et adaptabilité du fuseau mitotique. Vol. PhD. Univesité de rennes 1.

Mickey, B., and J. Howard. 1995. Rigidity of microtubules is increased by stabilizing agents. *The Journal of cell biology*. 130:909-917.

Moores, C.A., M. Perderiset, F. Francis, J. Chelly, A. Houdusse, and R.A. Milligan. 2004. Mechanism of microtubule stabilization by doublecortin. *Molecular cell*. 14:833-839.

Moores, C.A., M. Perderiset, C. Kappeler, S. Kain, D. Drummond, S.J. Perkins, J. Chelly, R. Cross, A. Houdusse, and F. Francis. 2006. Distinct roles of doublecortin modulating the microtubule cytoskeleton. *The EMBO Journal*. 25:4448-4457.

Nedelec, F., and D. Foethke. 2007. Collective Langevin dynamics of flexible cytoskeletal fibers. *New Journal of Physics*. 9:427.

Nguyen, M.M., M.C. Stone, and M.M. Rolls. 2011. Microtubules are organized independently of the centrosome in Drosophilaneurons. *Neural Development*. 6:38.

Nguyen-Ngoc, T., K. Afshar, and P. Gonczy. 2007. Coupling of cortical dynein and G[alpha] proteins mediates spindle positioning in Caenorhabditis elegans. *Nat Cell Biol*. 9:1294-1302.

Nishi, K., S. Raja, A. Pham, R. Freeman, A. Roll-Mecak, F.C. MacKintosh, and C.F. Schmidt. 2023. Nonequilibrium bending fluctuations reveal microtubule mechanics in-vivo and their regulation by glutamylation. *bioRxiv*:2023.2010.2026.564252.

Nishida, K., K. Matsumura, M. Tamura, T. Nakamichi, K. Shimamori, M. Kuragano, A.M.R. Kabir, A. Kakugo, S. Kotani, N. Nishishita, and K. Tokuraku. 2023. Effects of three microtubule-associated proteins (MAP2, MAP4, and Tau) on microtubules' physical properties and neurite morphology. *Scientific Reports*. 13:8870.

Oegema, K., and T. Hyman. 2006. Cell division. *WormBook: The Online Review of C. elegans Biology [Internet]*.

Pampaloni, F., G. Lattanzi, A. Jonáš, T. Surrey, E. Frey, and E.-L. Florin. 2006. Thermal fluctuations of grafted microtubules provide evidence of a length-dependent persistence length. *Proceedings of the National Academy of Sciences*. 103:10248-10253.

Papin, S., and P. Paganetti. 2020. Emerging Evidences for an Implication of the Neurodegeneration-Associated Protein TAU in Cancer. *Brain Sciences*. 10:862.

Pease, J.C., and J.S. Tirnauer. 2011. Mitotic spindle misorientation in cancer – out of alignment and into the fire. *Journal of Cell Science*. 124:1007-1016.

Pecreaux, J., S. Redemann, Z. Alayan, B. Mercat, S. Pastezeur, C. Garzon-Coral, A.A. Hyman, and J. Howard. 2016. The mitotic spindle in the one-cell C. elegans embryo is positioned with high precision and stability. *Biophys J*. 111:1773-1784.

Pécréaux, J., S. Redemann, Z. Alayan, B. Mercat, S. Pastezeur, C. Garzon-Coral, Anthony A. Hyman, and J. Howard. 2016. The Mitotic Spindle in the One-Cell C. elegans Embryo Is Positioned with High Precision and Stability. *Biophysical journal*. 111:1773-1784.

Pécréaux, J., J.-C. Röper, K. Kruse, F. Jülicher, A.A. Hyman, S.W. Grill, and J. Howard. 2006a. Spindle Oscillations during Asymmetric Cell Division Require a Threshold Number of Active Cortical Force Generators. *Current Biology*. 16:2111-2122.

Pécréaux, J., C. Zimmer, and J.-C. Olivo-Marin. 2006b. Biophysical active contours for cell tracking I: Tension and bending. *In* Image Processing, 2006 IEEE International Conference on. IEEE. 1949-1952.

Piehl, M., U.S. Tulu, P. Wadsworth, and L. Cassimeris. 2004. Centrosome maturation: measurement of microtubule nucleation throughout the cell cycle by using GFP-tagged EB1. *Proceedings of the National Academy of Sciences*. 101:1584-1588.

Pierre, D.A., and M.J. Lowe. 1975. Mathematical programming via augmented lagrangians: An introduction with computer programs. *(No Title)*.

Portran, D., L. Schaedel, Z. Xu, M. Théry, and Maxence V. Nachury. 2017. Tubulin acetylation protects long-lived microtubules against mechanical ageing. *Nature Cell Biology*. 19:391.

Quesada-Hernández, E., L. Caneparo, S. Schneider, S. Winkler, M. Liebling, S.E. Fraser, and C.-P. Heisenberg. 2010. Stereotypical Cell Division Orientation Controls Neural Rod Midline Formation in Zebrafish. *Current Biology*. 20:1966-1972.

Quyn, A.J., P.L. Appleton, F.A. Carey, R.J.C. Steele, N. Barker, H. Clevers, R.A. Ridgway, O.J. Sansom, and I.S. Näthke. 2010. Spindle Orientation Bias in Gut Epithelial Stem Cell Compartments Is Lost in Precancerous Tissue. *Cell Stem Cell*. 6:175-181.

Redemann, S., J. Baumgart, N. Lindow, M. Shelley, E. Nazockdast, A. Kratz, S. Prohaska, J. Brugués, S. Fürthauer, and T. Müller-Reichert. 2017. C. elegans chromosomes connect to centrosomes by anchoring into the spindle network. *Nature Communications*. 8:15288.

Redemann, S., J. Pecreaux, N.W. Goehring, K. Khairy, E.H.K. Stelzer, A.A. Hyman, and J. Howard. 2010. Membrane invaginations reveal cortical sites that pull on mitotic spindles in one-cell C. elegans embryos. *PloS one*. 5:e12301.

Reiner, O., F.M. Coquelle, B. Peter, T. Levy, A. Kaplan, T. Sapir, I. Orr, N. Barkai, G. Eichele, and S. Bergmann. 2006. The evolving doublecortin (DCX) superfamily. *BMC genomics*. 7:188.

Rizzelli, F., M.G. Malabarba, S. Sigismund, and M. Mapelli. 2020. The crosstalk between microtubules, actin and membranes shapes cell division. *Open Biology*. 10:190314.

Robison, P., M.A. Caporizzo, H. Ahmadzadeh, A.I. Bogush, C.Y. Chen, K.B. Margulies, V.B. Shenoy, and B.L. Prosser. 2016. Detyrosinated microtubules buckle and bear load in contracting cardiomyocytes. *Science*. 352:aaf0659.

Rossi, G., L. Dalprà, F. Crosti, S. Lissoni, F.L. Sciacca, M. Catania, G. Di Fede, M. Mangieri, G. Giaccone, D. Croci, and F. Tagliavini. 2008. A new function of microtubule-associated protein tau: involvement in chromosome stability. *Cell Cycle*. 7:1788-1794.

Rossi, G., V. Redaelli, P. Contiero, S. Fabiano, G. Tagliabue, P. Perego, L. Benussi, A.C. Bruni, G. Filippini, and M. Farinotti. 2018. Tau mutations serve as a novel risk factor for cancer. *Cancer research*. 78:3731-3739.

Saleh, J., M.-A. Fardin, A. Barai, M. Soleilhac, O. Frenoy, C. Gaston, H. Cui, T. Dang, N. Gaudin, A. Vincent, N. Minc, and D. Delacour. 2023. Length limitation of astral microtubules orients cell divisions in murine intestinal crypts. *Developmental Cell*. 58:1519-1533.e1516.

Sandberg, K., and M. Brega. 2007. Segmentation of thin structures in electron micrographs using orientation fields. *Journal of Structural Biology*. 157:403-415.

Schaedel, L., S. Triclin, D. Chrétien, A. Abrieu, C. Aumeier, J. Gaillard, L. Blanchoin, M. Théry, and K. John. 2019. Lattice defects induce microtubule self-renewal. *Nature Physics*.

Schindelin, J., I. Arganda-Carreras, E. Frise, V. Kaynig, M. Longair, T. Pietzsch, S. Preibisch, C. Rueden, S. Saalfeld, B. Schmid, J.-Y. Tinevez, D.J. White, V. Hartenstein, K. Eliceiri, P. Tomancak, and A. Cardona. 2012. Fiji: an open-source platform for biological-image analysis. *Nature methods*. 9:676-682.

Schneider, M.W.G., B.A. Gibson, S. Otsuka, M.F.D. Spicer, M. Petrovic, C. Blaukopf, C.C.H. Langer, P. Batty, T. Nagaraju, L.K. Doolittle, M.K. Rosen, and D.W. Gerlich. 2022. A mitotic chromatin phase transition prevents perforation by microtubules. *Nature*.

Sébastien, M., E.N.P. Prowse, A.G. Hendricks, and G.J. Brouhard. 2023. Doublecortin regulates neuronal migration by editing the tubulin code. *bioRxiv*:2023.2006.2002.543327.

Shu, T., H.-C. Tseng, T. Sapir, P. Stern, Y. Zhou, K. Sanada, A. Fischer, F.M. Coquelle, O. Reiner, and L.-H. Tsai. 2006. Doublecortin-like kinase controls neurogenesis by regulating mitotic spindles and M phase progression. *Neuron*. 49:25-39.

Siller, K.H., C. Cabernard, and C.Q. Doe. 2006. The NuMA-related Mud protein binds Pins and regulates spindle orientation in Drosophila neuroblasts. *Nature Cell Biology*. 8:594-600.

Singh, D., N. Schmidt, F. Müller, T. Bange, and A.W. Bird. 2021. Destabilization of Long Astral Microtubules via Cdk1-Dependent Removal of GTSE1 from Their Plus Ends Facilitates Prometaphase Spindle Orientation. *Current Biology*. 31:766-781.e768.

Soler, N., L. Chesneau, H. Bouvrais, S. Pastezeur, L. Le Marrec, and J. Pecreaux. 2022. Kinetochore microtubules flux poleward along fixed centrosome-anchored microtubules during the metaphase of C. elegans one-cell embryo. *bioRxiv*:2022.2011.2007.515476.

Srayko, M., A. Kaya, J. Stamford, and A.A. Hyman. 2005. Identification and Characterization of Factors Required for Microtubule Growth and Nucleation in the Early C. elegans Embryo. *Developmental Cell*. 9:223-236.

Stiess, M., N. Maghelli, L.C. Kapitein, S. Gomis-Rüth, M. Wilsch-Bräuninger, C.C. Hoogenraad, I.M. Tolić-Nørrelykke, and F. Bradke. 2010. Axon Extension Occurs Independently of Centrosomal Microtubule Nucleation. *Science*. 327:704-707.

Strauss, B., R.J. Adams, and N. Papalopulu. 2006. A default mechanism of spindle orientation based on cell shape is sufficient to generate cell fate diversity in polarised Xenopus blastomeres.

Sugioka, K., L.-E. Fielmich, K. Mizumoto, B. Bowerman, S. van den Heuvel, A. Kimura, and H. Sawa. 2018. Tumor suppressor APC is an attenuator of spindle-pulling forces during C. elegans asymmetric cell division. *Proceedings of the National Academy of Sciences*:201712052.

Sui, H., and K.H. Downing. 2010. Structural basis of interprotofilament interaction and lateral deformation of microtubules. *Structure*. 18:1022-1031.

Théry, M., and L. Blanchoin. 2021. Microtubule self-repair. *Current Opinion in Cell Biology*. 68:144-154.

Thomas, G.E., M.R. Renjith, and T.K. Manna. 2017. Kinetochore–microtubule interactions in chromosome segregation: lessons from yeast and mammalian cells. *Biochemical Journal*. 474:3559-3577.

Tint, I., D. Jean, P.W. Baas, and M.M. Black. 2009. Doublecortin associates with microtubules preferentially in regions of the axon displaying actin-rich protrusive structures. *Journal of Neuroscience*. 29:10995-11010.

Tintori, Sophia C., E. Osborne Nishimura, P. Golden, Jason D. Lieb, and B. Goldstein. 2016. A Transcriptional Lineage of the Early C. elegans Embryo. *Developmental Cell*. 38:430-444.

Tsou, M.F.B., A. Hayashi, L.R. DeBella, G. McGrath, and L.S. Rose. 2002. LET-99 determines spindle position and is asymmetrically enriched in response to PAR polarity cues in C. elegans embryos. *Development*. 129:4469-4481.

van Leen, E.V., F. di Pietro, and Y. Bellaïche. 2020. Oriented cell divisions in epithelia: from force generation to force anisotropy by tension, shape and vertices. *Current Opinion in Cell Biology*. 62:9-16.

Venier, P., A.C. Maggs, M.-F. Carlier, and D. Pantaloni. 1994. Analysis of microtubule rigidity using hydrodynamic flow and thermal fluctuations. *Journal of biological chemistry*. 269:13353-13360.

Vreugdenhil, E., S.M. Kolk, K. Boekhoorn, C.P. Fitzsimons, M. Schaaf, T. Schouten, A. Sarabdjitsingh, R. Sibug, and P.J. Lucassen. 2007. Doublecortin-like, a microtubule-associated protein expressed in radial glia, is crucial for neuronal precursor division and radial process stability. *European Journal of Neuroscience*. 25:635-648.

Wall, K.P., H. Hart, T. Lee, C. Page, T.L. Hawkins, and L.E. Hough. 2020. C-Terminal Tail Polyglycylation and Polyglutamylation Alter Microtubule Mechanical Properties. *Biophysical journal*. 119:2219-2230.

Williams, S.E., S. Beronja, H.A. Pasolli, and E. Fuchs. 2011. Asymmetric cell divisions promote Notch-dependent epidermal differentiation. *Nature*. 470:353-358.

Wood, W.B., R. Hecht, S. Carr, R. Vanderslice, N. Wolf, and D. Hirsh. 1980. Parental effects and phenotypic characterization of mutations that affect early development in Caenorhabditis elegans. *Developmental Biology*. 74:446-469.

Woodruff, J.B., O. Wueseke, V. Viscardi, J. Mahamid, S.D. Ochoa, J. Bunkenborg, P.O. Widlund, A. Pozniakovsky, E. Zanin, S. Bahmanyar, A. Zinke, S.H. Hong, M. Decker, W. Baumeister,

J.S. Andersen, K. Oegema, and A.A. Hyman. 2015. Regulated assembly of a supramolecular centrosome scaffold in vitro. *Science*. 348:808-812.

Wu, H.-Y., G. Kabacaoğlu, E. Nazockdast, H.-C. Chang, M.J. Shelley, and D.J. Needleman. 2021. Laser Ablation and Fluid Flows Show a Single Force Mechanism Governs Spindle Positioning. *bioRxiv*:2021.2011.2021.469320.

Wu, J.C., and L.S. Rose. 2007. PAR-3 and PAR-1 inhibit LET-99 localization to generate a cortical band important for spindle positioning in Caenorhabditis elegans embryos. *Molecular biology of the cell*. 18:4470-4482.

Xu, Z., L. Schaedel, D. Portran, A. Aguilar, J. Gaillard, M.P. Marinkovich, M. Théry, and M.V. Nachury. 2017. Microtubules acquire resistance from mechanical breakage through intralumenal acetylation. *Science*. 356:328-332.

Zhang, Z., Y. Nishimura, and P. Kanchanawong. 2017. Extracting microtubule networks from superresolution single-molecule localization microscopy data. *Molecular biology of the cell*. 28:333-345.

Supplemental figures, movies, tables and files

To the article: "Microtubule stiffening by doublecortin-domain protein ZYG-8 contributes to spindle orientation during *C. elegans* zygote division"; Cueff L. *et al.*, 2024.

Table of Contents

1- Supplemental figures *2*

2- Supplemental movies *16*

3- Supplemental tables *17*

4- Supplemental files *21*

5- References *21*

1- Supplemental figures

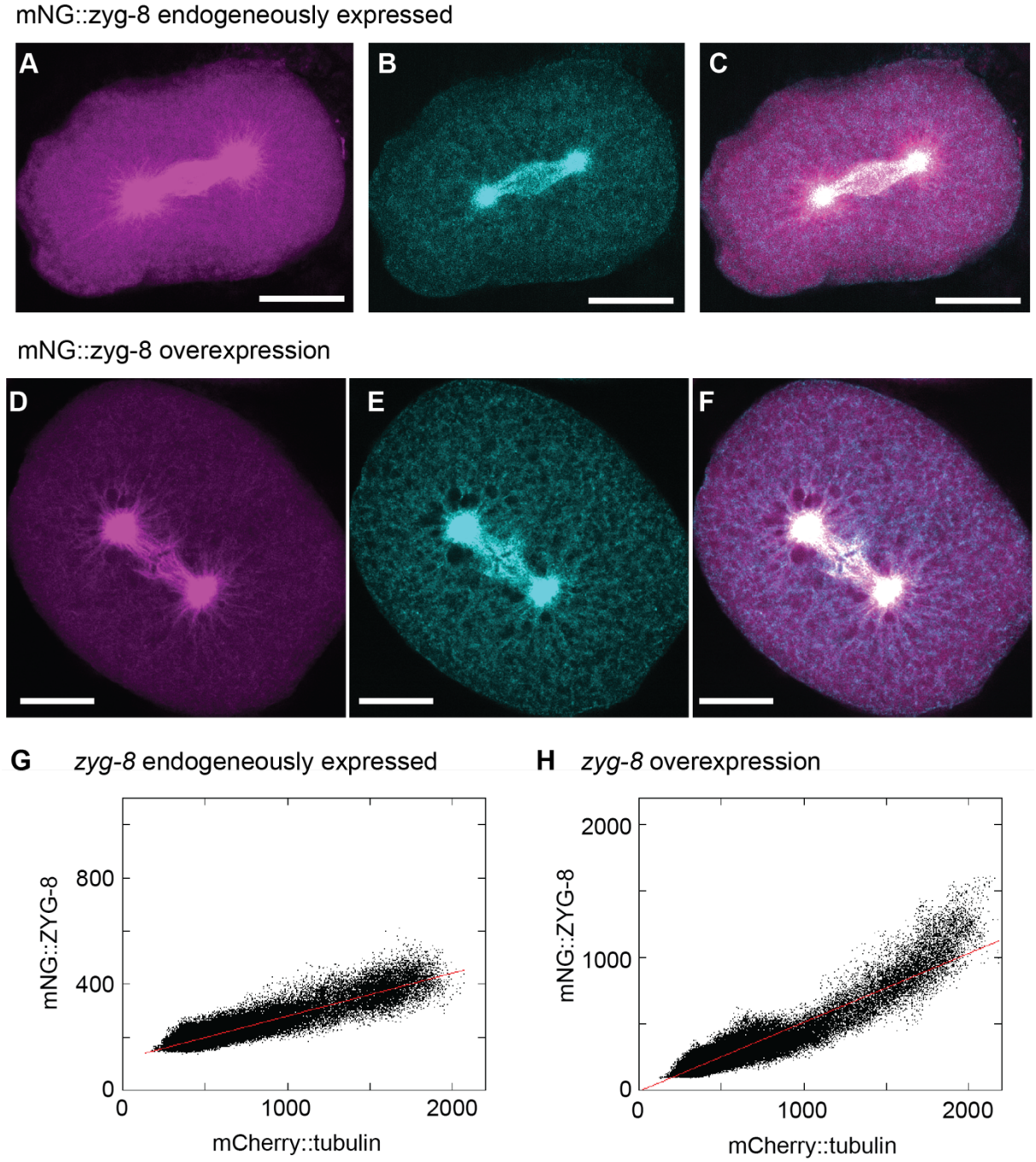

Figure S1: mNG::ZYG-8 colocalises with mCherry::tubulin on both astral and spindle microtubules. (**A-C**) Exemplar fixed embryo in metaphase displaying (A) fluorescent labelling of microtubules (mCherry::tubulin) and (B) mNG::ZYG-8, imaged using deconvolved confocal microscopy (Methods M3 & M4). (C) Merged view of (A) and (B), revealing colocalisation in white. (**D-F**) Exemplar fixed embryo overexpressing *zyg-8* in metaphase displaying (D) fluorescent labelling of microtubules (mCherry::tubulin) and (E) mNG::ZYG-8, imaged using deconvolved confocal microscopy. (F) Merged view of (D) and (E), revealing colocalisation in white. (**G-H**) Scatter plots of the fluorescent intensities (G) from the two channels shown in (A-B) and (H) from the two channels shown in (D-E). The Pearson correlation coefficients are (G) $r = 0.89$ ($p > 0.95$) and (H) $r = 0.93$ ($p > 0.95$), indicating significant colocalisation (Method M5). Scale bars represent 10 μm.

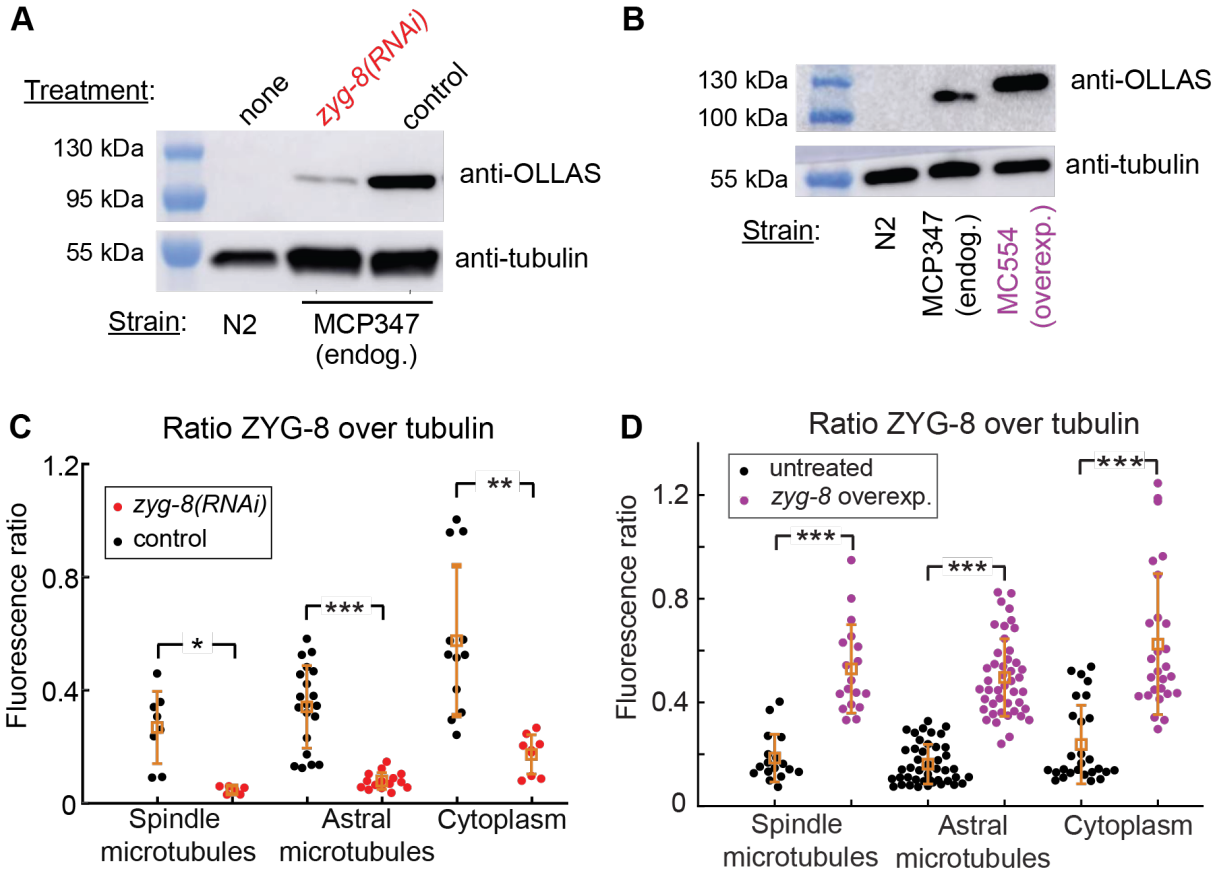

Figure S2: ZYG-8 localisation on the astral and spindle microtubules correlates with its expression level.

(A-B) Western blots of worm lysates showing OLLAS and tubulin levels: (A) *zyg-8(RNAi)* treatment compared to control treatment (empty vector L4440) using *3*OLLAS::zyg-8* endogenous strain MCP437; (B) *pPie-1::mNG::3*OLLAS::zyg-8* overexpressing strain MCP554 compared to MCP347 strain (Method M6). Wild-type N2 strain was used as a negative control. (**C-D**) Fluorescence ratio of mNG::ZYG-8 over mCherry::tubulin : (C) (red) *N* = 4 *zyg-8(RNAi)* treated embryos and (black) *N* = 4 control embryos; (D) (purple) *N* = 9 *zyg-8* overexpressing embryos and (black) *N* = 9 untreated embryos. Fluorescence measurements were performed on spindle microtubules (2 measurements per embryo), on astral microtubules (5 measurements per embryo) and in the cytoplasm (3 measurements per embryo) (Methods M3, M4 and M6). The orange squares and error bars correspond to the means and SD (Method M14).

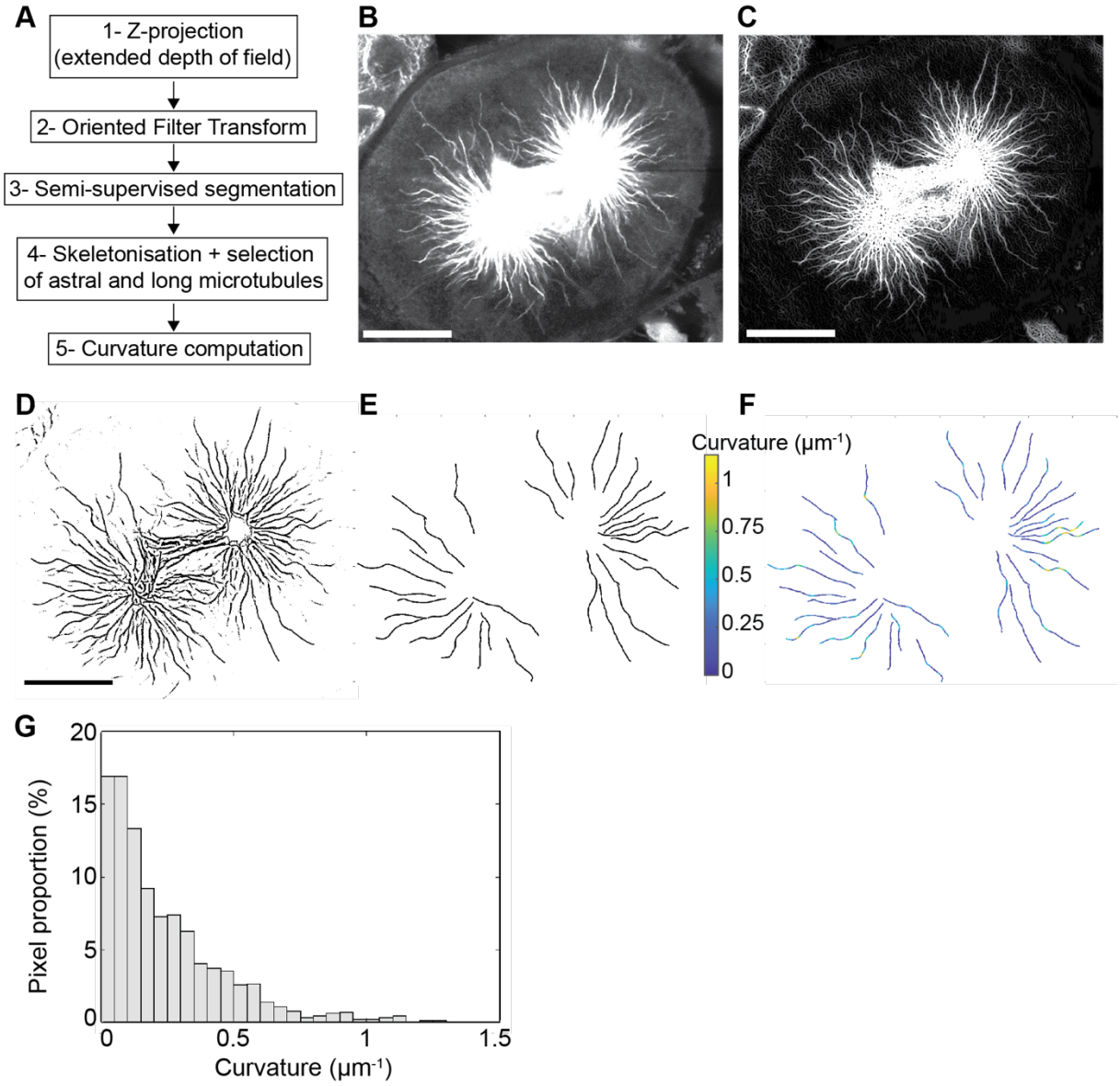

Figure S3: Image processing pipeline mapping the curvatures of astral microtubules.
(**A**) Flow diagram of the pipeline assembled to quantify the local curvatures of the astral microtubules (Method M7). (**B-F**) Exemplar analysis of *zyg-8(or484ts)* mutant fixed embryo at the restrictive temperature with α-tubulin immunostaining: (B) the extended depth of field over three successive z-planes (C) is processed using the Oriented Filter Transform (OFT). (D) Segmentation is performed using the semi-supervised method *Ilastik* to generate the binary image. (E) This image is then skeletonised, focusing on astral filaments longer than 4 μm. (F, G) Local curvatures are calculated along each filament and (F) displayed into a colour-encoded curvature map. (G) We also generated the local curvature distribution. Scale bars represent 10 μm.

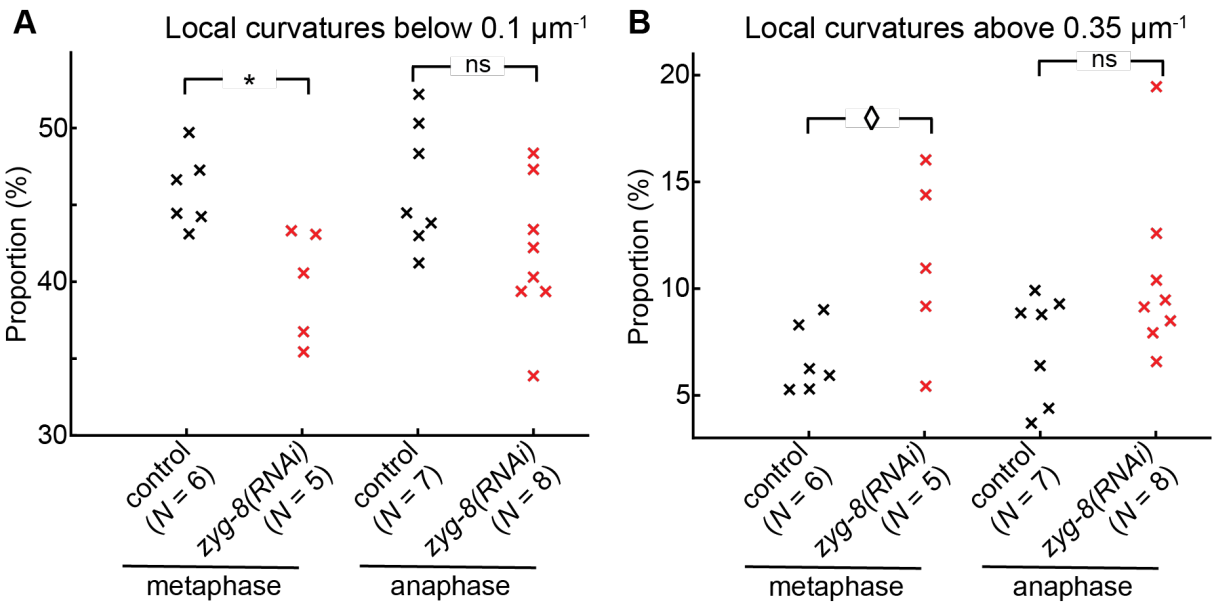

Figure S4: Upon *zyg-8(RNAi)*, the astral microtubules show a slightly greater proportion of high local curvatures during metaphase.

Proportions of (**A**) low local curvatures (below 0.1 μm^{-1}) and (**B**) high local curvatures (above 0.35 μm^{-1}) along the astral microtubules for (red) *zyg-8(RNAi)* treated embryos and (black) control embryos in metaphase and anaphase (Methods M7 and M14). *N* represents the number of z-projected sections for each condition studied. Data are the same as for Figure 2A-B.

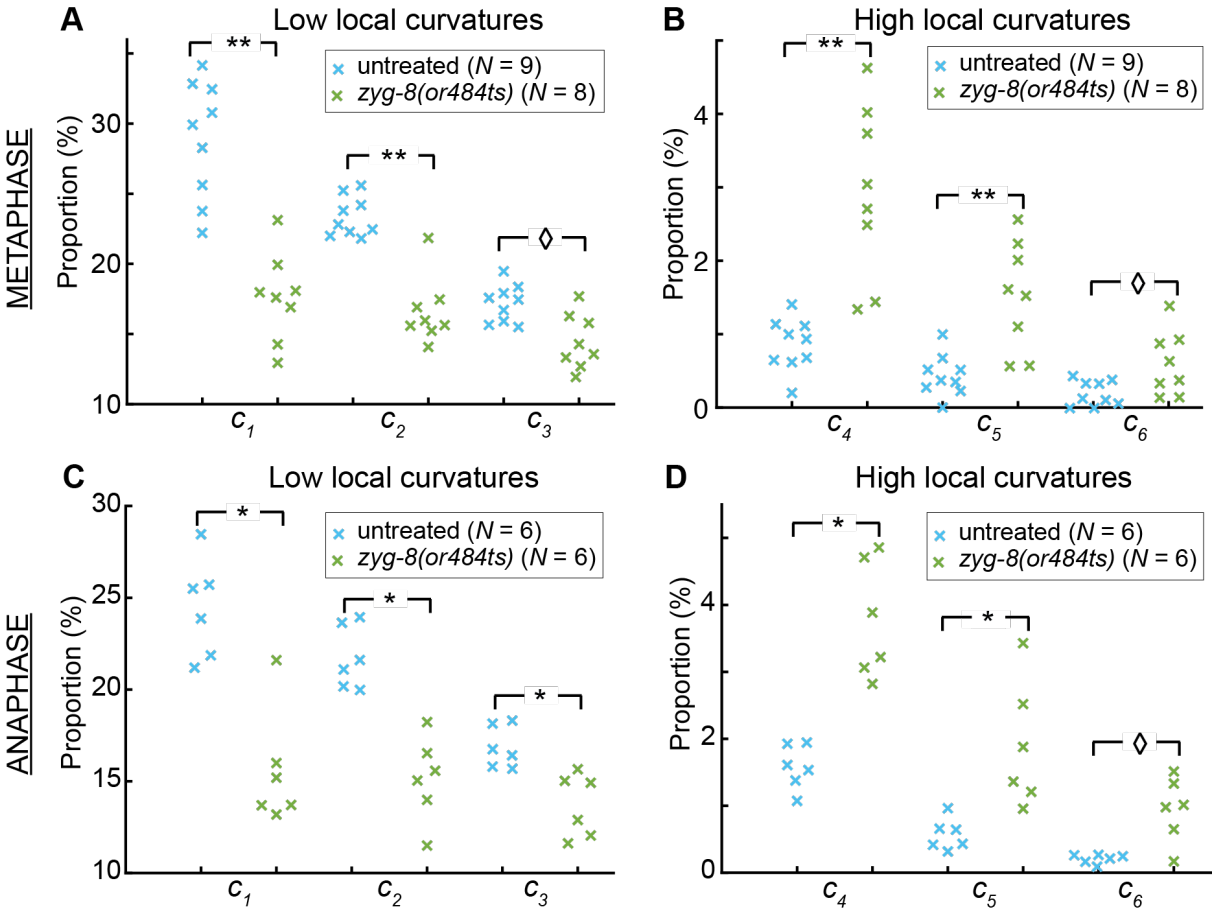

Figure S5: In *zyg-8(or484ts)* mutants at the restrictive temperature, the astral microtubules show an increased proportion of high local curvatures.

Proportions of (A, C) low local curvatures ($0 \leq C_1 < 0.05$ µm^{-1}; $0.05 \leq C_2 < 0.1$ µm^{-1}; $0.1 \leq C_3 < 0.15$ µm^{-1}) and (B, D) high local curvatures ($0.4 \leq C_4 < 0.45$ µm^{-1}; $0.5 \leq C_5 < 0.55$ µm^{-1}; $0.6 \leq C_6 < 0.65$ µm^{-1}) along the astral microtubules for (light green) *zyg-8(or484ts)* mutants and (light blue) untreated embryos, both at the restrictive temperature, (A-B) during metaphase and (C-D) during anaphase (Methods M7 and M14). *N* represents the number of z-projected sections for each condition studied. Data are the same as for Figure 2C-D.

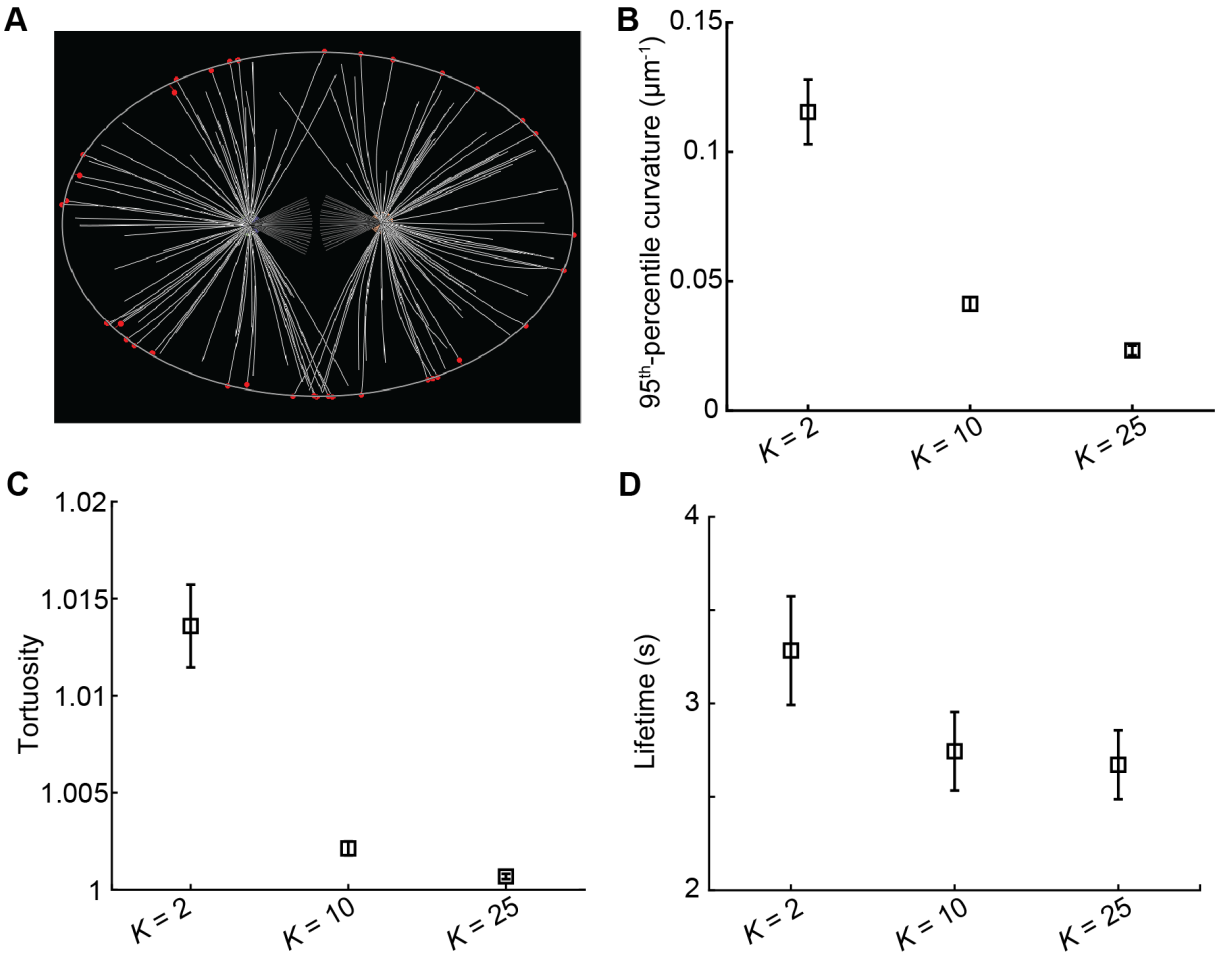

Figure S6: *In silico,* decreasing microtubule flexural rigidity increases microtubule cortical lifetimes. (**A**) *Cytosim* agent-centred simulation snapshot showing fibres mimicking microtubules in white, with cortical contacts depicted as red dots (Table S2, Method M8). (**B-D**) Simulation of astral microtubules of *C. elegans* mitosis with three different microtubule flexural rigidities (K = 2, 10 and 25 pN.µm^2): (B) medians of the highest curvatures (95th percentile), (C) medians of the tortuosity, both calculated from the entire set of microtubules 45 seconds after starting the simulation and (D) cortical lifetimes of the astral microtubules, collected along each simulation run beginning 15 seconds after the simulation started to allow for warm-up. The black squares and error bars correspond to the means and SD over 40 simulations per condition.

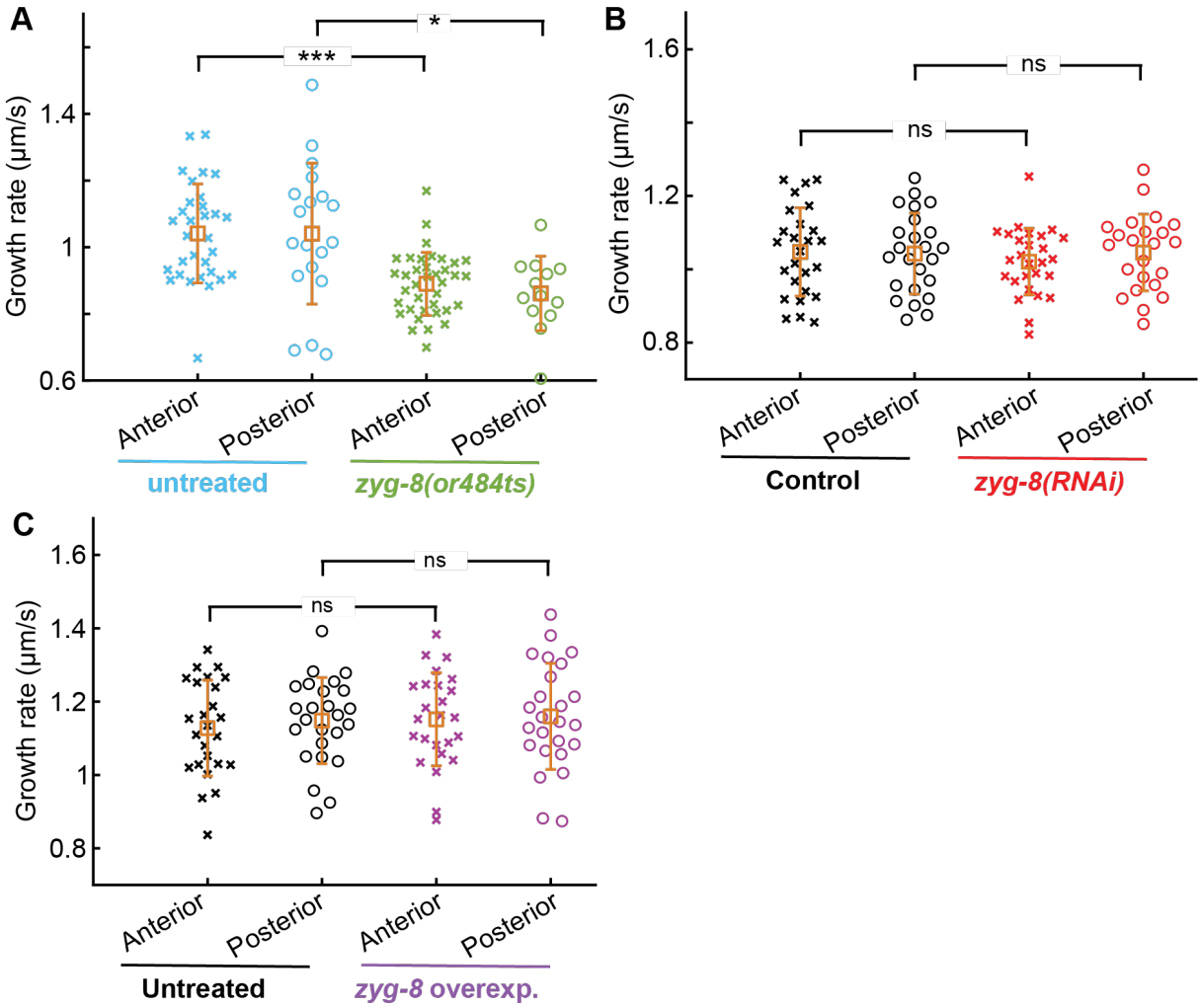

Figure S7: Astral microtubule growth rate is reduced only in *zyg-8(or484ts)* mutants.
Growth rates of astral microtubules measured at (cross) anterior and (circle) posterior centrosomes using EBP-2::mKate2 labelling (Method M10): (**A**) (light green) *N* = 37 comets from microtubules emanating from the anterior centrosome and *N* = 13 comets from posterior centrosome, in 10 *zyg-8(or484ts)* mutants, and (light blue) *N* = 31 comets from anterior-centrosome and *N* = 19 posterior-centrosome comets in 13 untreated embryos, both at the restrictive temperature; (**B**) (red) *N* = 27 comets from anterior centrosome and *N* = 23 comets from posterior centrosome in 10 *zyg-8(RNAi)* treated embryos, and (black) *N* = 26 comets from anterior centrosome and *N* = 24 comets from posterior centrosome in 8 control embryos; (**C**) (purple) *N* = 25 comets from anterior centrosome and *N* = 25 comets from posterior centrosome in 10 *zyg-8* overexpressing embryos and (black) *N* = 25 comets from anterior centrosome and *N* = 25 comets from posterior centrosome in 10 untreated embryos. The orange squares and error bars correspond to the means and SD (Method M14).

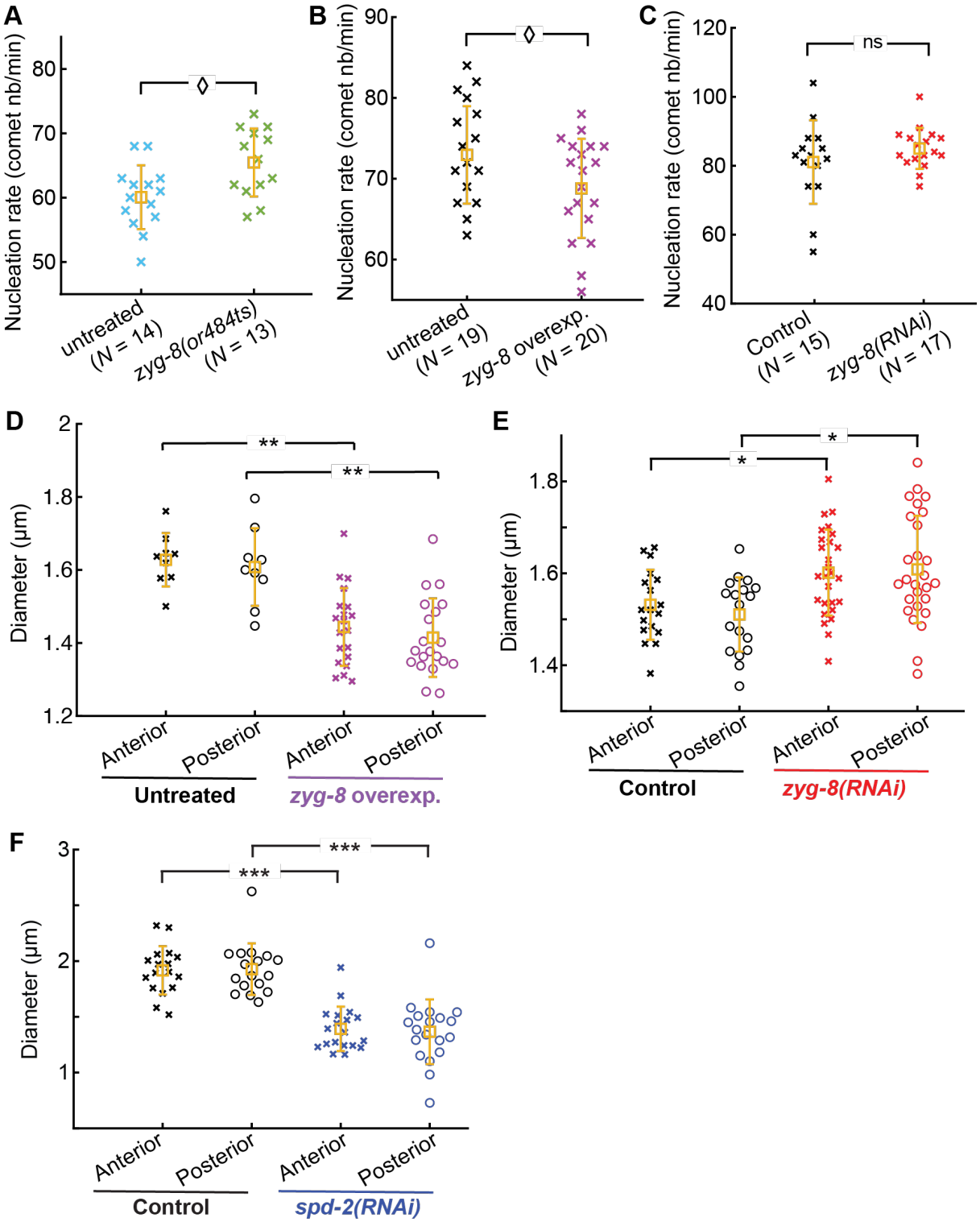

Figure S8: ZYG-8 mildly regulates astral microtubule nucleation rate.

(A-C) Nucleation rates of the astral microtubules measured using EBP-2::mKate2 labelling with *N* indicating the number of analysed centrosomes per condition (Method M10): (A) (light green) N_e = 8 *zyg-8(or484ts)* mutants and (light blue) N_e = 9 untreated embryos, both at the restricted temperature; (B) (purple) N_e = 10 *zyg-8* overexpressing embryos and (black) N_e = 10 untreated embryos; (C) (red) N_e = 10 *zyg-8(RNAi)* treated embryos and (black) N_e = 8 control embryos. (**D-F**) Diameter during metaphase of (cross) anterior and (circle) posterior centrosomes using (D-E) mCherry::TBG-1 or (F) TBG-1::GFP labelled strains (Method M12): (D) (purple) N_e = 21 *zyg-8* overexpressing embryos and

(black) N_e = 9 untreated embryos; (E) (red) N_e = 27 *zyg-8(RNAi)* treated embryos and (black) N_e = 18 control embryos; (F) (blue) N_e = 19 *spd-2(RNAi)* treated embryos and (black) N_e = 17 control embryos. The orange squares and error bars correspond to the means and SD (Method M14).

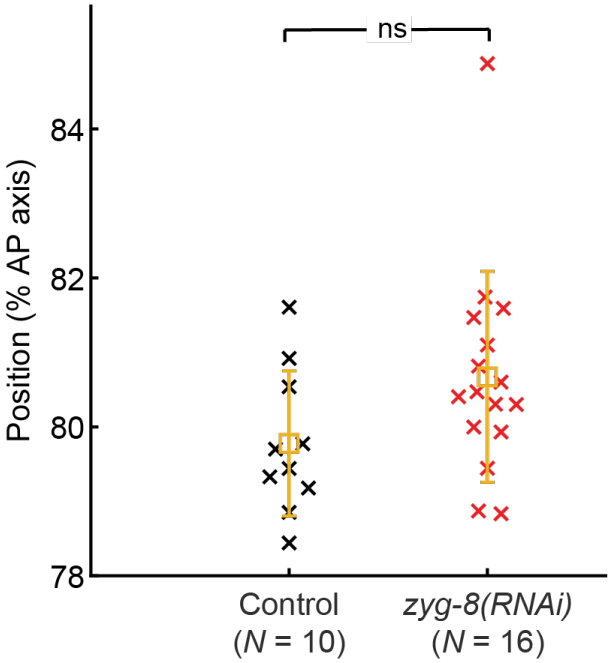

Figure S9: Upon *zyg-8(RNAi),* the most-posterior position of the posterior centrosome does not vary significantly.

Most-posterior positions of the posterior centrosome for (red) *N* = 16 *zyg-8(RNAi)* treated embryos and (black) *N* = 10 control embryos. We tracked and analysed the centrosomes of embryos carrying a GFP::TBB-2 fluorescent label (Method M11). Embryos are the same as in Figure 5A-B. The orange squares and error bars correspond to the means and SD (Method M14).

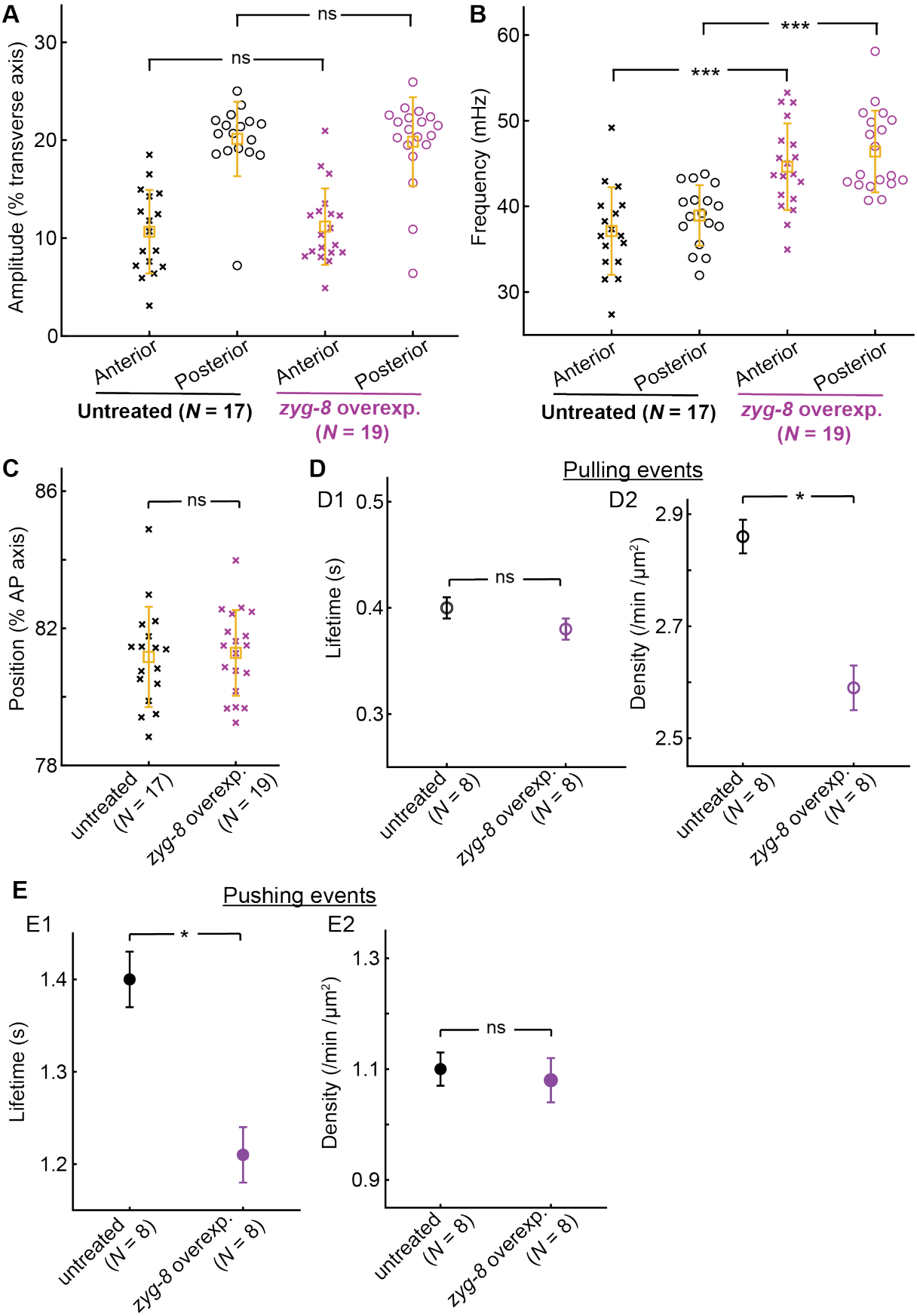

Figure S10: Overexpressing *zyg-8* does not affect the amplitudes of spindle pole oscillations.
(**A**) Maximal amplitudes of spindle pole oscillations, (**B**) frequencies of the oscillations, and (**C**) most-posterior positions of the posterior centrosome during anaphase. We tracked and analysed the

centrosomes labelled by mCherry::TBG-1: (purple) *N* = 19 *zyg-8* overexpressing embryos and (black) *N* = 17 untreated embryos (Method M11). The orange squares and error bars correspond to the means and SD (Method M14). (**D**) Lifetimes and densities of the cortical pulling events, and (**E**) lifetimes and densities of the cortical pushing events. We tracked and analysed the microtubule contacts at the cell cortex using a mCherry::tubulin fluorescent labelling: (purple) *N* = 8 *zyg-8* overexpressing embryos and (black) *N* = 8 untreated embryos (same embryos as in Figure 4D-F, Method M9).

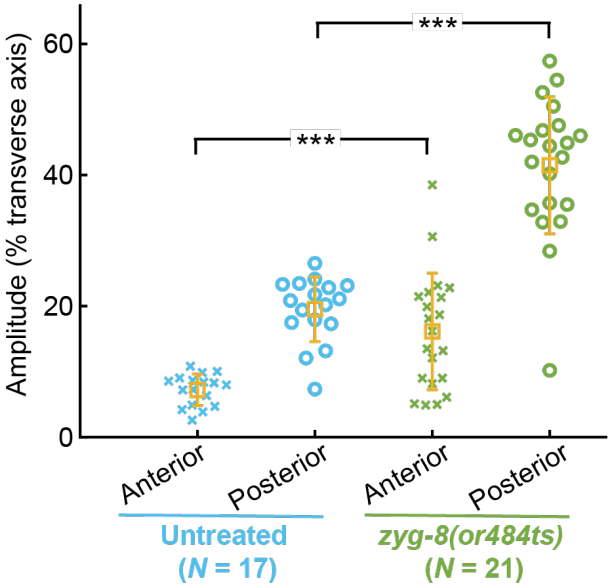

Figure S11: Spindle pole oscillations are exaggerated *in zyg-8(or484ts)* mutants.
Maximal amplitudes of the spindle pole oscillations for (light green) *N* = 21 *zyg-8(or484ts)* mutants and (light blue) *N* = 17 untreated embryos, both at the restrictive temperature. We tracked and analysed the centrosomes labelled by EBP-2::mKate2 (Method M11). The orange squares and error bars correspond to the means and SD (Method M14).

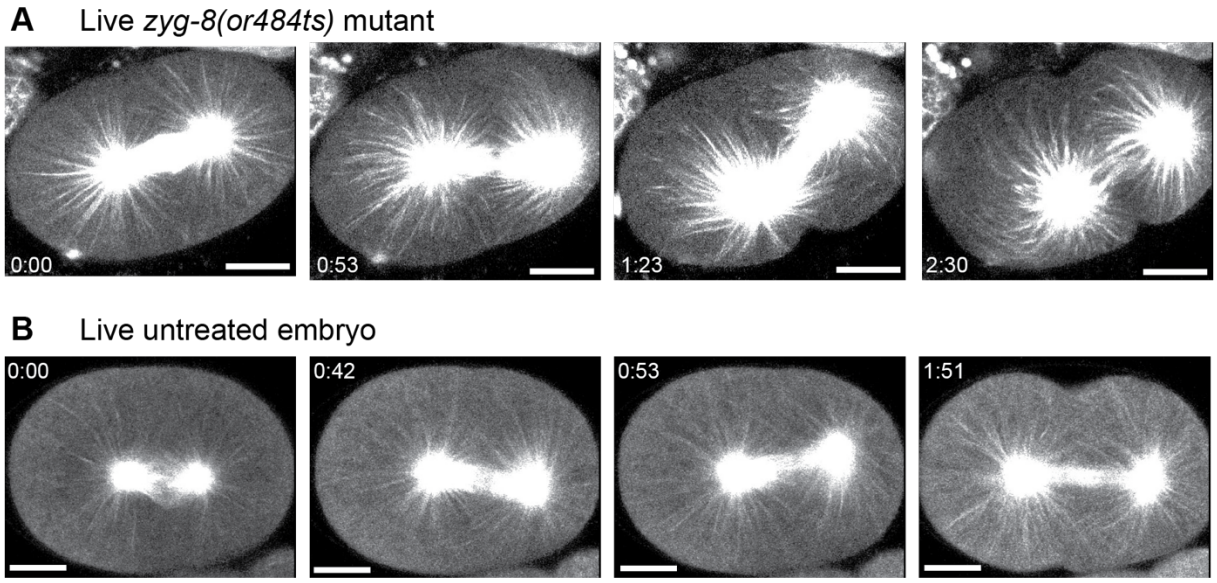

Figure S12: In *zyg-8(or484ts)* mutants, astral microtubules are long enough to reach the cell cortex. Time-lapse Kalman-filtered deconvolved images along anaphase of (**A**) an exemplar *zyg-8(or484ts)* mutant and (**B**) an exemplar untreated embryo, both at the restrictive temperature. Microtubules were labelled by GFP::TBB-2. Time is indicated from anaphase onset in min:sec. Scale bars represent 10 μm. These time-lapse images are sourced from (A) the movie S4 and (B) the movie S6.

2- Supplemental movies

The movies can be downloaded using the following link:
https://sdrive.cnrs.fr/s/Q7MWSRHRAn3Nrir

Movie S1: Exemplar simulation with the rigidity of astral microtubule set to 2 pN·µm² (Method M8).

Movie S2: Exemplar simulation with the rigidity of astral microtubule set to 10 pN·µm² (Method M8).

Movie S3: Exemplar simulation with the rigidity of astral microtubule set to 25 pN·µm² (Method M8).

Movie S4: Exemplar live *zyg-8(or484ts)* mutant at the restrictive temperature with fluorescently labelled microtubules (GFP::TBB-2) imaged using a deconvolved confocal microscope at the spindle plane (Methods M3 and M4). We denoised the movie using Kalman filtering, with the gain set to 0.5 and the initial noise set to 0.05. The images shown in Figure S12A were taken from this movie. The movie is 5-times accelerated.

Movie S5: Exemplar live *zyg-8(or484ts)* mutant at the restrictive temperature with fluorescently labelled microtubules (GFP::β-TBB-2) imaged using a deconvolved confocal microscope at the spindle plane (Methods M3 and M4). We denoised the movie using Kalman filtering, with the gain set to 0.5 and the initial noise set to 0.05. The movie is 5-times accelerated.

Movie S6: Exemplar live untreated embryo at the restrictive temperature with fluorescently labelled microtubules (GFP::TBB-2) imaged using a deconvolved confocal microscope at the spindle plane (Methods M3 and M4). We denoised the movie using Kalman filtering, with the gain set to 0.5 and the initial noise set to 0.05. The images shown in Figure S12B were taken from this movie. The movie is 5-times accelerated.

3- Supplemental tables

	Genotype description	If crossing, from which strains	Origin & Reference
MCP347 4x*	zyg-8(bab347[3xOLLAS::zyg-8]) III		This study
MCP361 4x*	zyg-8(bab361[mNG::zyg-8]) III		This study
MCP554 2x**	ttTi5605(bab516; bab554[pPie-1::mNG::3*OLLAS::zyg-8::3'UTR tbb-2] II)		This study
TH430	ddIs14[pie-1p::EBP-2::GFP; unc-119(+)]; weIs21[Ppie-1::mCherry::tub::pie-1 3'UTR]	TH66 crossed with JA1559	TH66: (Srayko et al., 2005) JA1559: Ahringer lab
JEP153	weIs21[Ppie-1::mCherry::tub::pie-1 3'UTR]	Out-crossing of TH430	TH430: Hyman lab.
JEP170	zyg-8(bab361[mNG::zyg-8]) III; weIs21[Ppie-1::mCherry::tub::pie-1 3'UTR]	JEP153 crossed with MCP361 4x	This study
JEP187	ttTi5605(bab516; bab554[pPie-1::mNG::3*OLLAS::zyg-8::3'UTR tbb-2])II; weIs21[Ppie-1::mCherry::tub::pie-1 3?UTR]	JEP153 crossed with MCP554 2x	This study
JEP97	unc-119(ed3) ? III; ltIs37 [pAA64; pie-1/mCHERRY::his-58; unc-119 (+)]IV;ddIs44[WRM0614cB02 GLCherry::tbg-1;unc-119(+)]	OD56 crossed with TH169	OD56: (McNally et al., 2006) TH169: (Woodruff et al., 2015)
JEP188	t ttTi5605(bab516; bab554[pPie-1::mNG::3*OLLAS::zyg-8::3'UTR tbb-2])II; unc-119(ed3) ? III; ltIs37 [pAA64; pie-1/mCHERRY::his-58; unc-119 (+)]IV;ddIs44[WRM0614cB02 GLCherry::tbg-1;unc-119(+)]	JEP97 crossed with MCP554	This study
EU3068	ebp-2(or1954[ebp-2::mKate2]) II; ruIs57[pie-1::GFP::tbb-2 +unc-119(+)] V		(Sugioka et al., 2018)
JEP180	zyg-8(or484) III; ebp-2(or1954[ebp-2::mKate2]) II	EU3068 crossed with EU924	EU924: (Encalada et al., 2000)
JEP10	such-1(h1960) III; unc-46(e177) mdf-1(gk2) V. ddIs180[WRM062cF05 spd-2:: 2xTY1 GFP FRT 3xFlag;unc-119(+)]	KR4012 crossed with TH231	KR4012: (Tarailo et al., 2007) TH231: (Decker et al., 2011)
JEP15	ddIs180[WRM062cF05 spd-2:: 2xTY1 GFP FRT 3xFlag;unc-119(+)] ltIs37 [pie-1p::mCherry::his-58 (pAA64) + unc-119(+)] IV	JEP10 crossed with OD56	This study

JEP183	zyg-8(or484) III ; ddIs180[WRM062cF05 spd-2:: 2xTY1 GFP FRT 3xFlag;unc-119(+)] ltIs37 [pie-1p::mCherry::his-58 (pAA64) + unc-119(+)] IV	JEP15 crossed with EU924	EU924: (Encalada et al., 2000)
AZ244	unc-119(ed3) III; ruIs57[pie-1::GFP::tbb-2 +unc-119(+)] V		(Praitis et al., 2001)
JEP82	ebp-2(or1954[ebp-2::mKate2]) II	Out-crossing of EU3068	This study
JEP193	ttTi5605(bab516; bab554[pPie-1::mNG::3*OLLAS::zyg-8::3'UTR tbb-2] II); ebp-2(or1954[ebp-2::mKate2]) II	JEP82 crossed with MCP554	This study
TH27	unc-119(ed3) III; ddIs6 [Ppie-1::GFP::tbg-1; unc-119(+)] V		(Oegema et al., 2001)

Table S1: List of the strains used in this study.
(* 4-times backcrossed; ** 2-times backcrossed.)

Object type	Characteristic parameters	Reference
Space: ellipse	Radii: 24.5 μm and 16.5 μm Viscosity: 5 Pa.s	(Daniels et al., 2006)
2 solids (that mimic anterior and posterior centrosomes)	External force: Anterior: 180 pN; posterior: 300 pN	(Grill et al., 2003)
2 asters with two fibre types	Initial position: Anterior: -5.6 μm; Posterior 4.7 μm from ellipse centre	*In vivo* measurements of the lab
Fibre, type #1 (spindle)	Activity: static Number per aster: 20 Initial length 6 μm Rigidity: 100 pN.μm^2 Position: 60°, radial distribution	
Fibre, type #2 (astral)	Activity: dynamic Number per aster: 75 Initial length 8 $\pm$ 6 μm Rigidity: 5, 10, 25 pN.μm^2 Position: 240°, random radial distribution Growing force: 1.67 pN Minimal length: 0.005 μm Growing speed: 0.71 μm/s Shrinking sped: -0.84 μm/s Catastrophe rate: 0.05 (no force); 0.5 (stall force) Rescue rate: 0.15	(Dogterom and Yurke, 1997; Srayko et al., 2005)
Single with hands	Activity: bind Anchored to a fixed position Unbinding rate: 0.1 Unbinding force: 5 pN	

Table S2: Objects and their parameters used in the three *Cytosim* simulations.

Conditions	Frequency interval	D (m^2/s)	f_c (Hz)	f_0 (Hz)
RNAi control (N = 15)	0.03 -> 0.3 Hz	1.7×10^{-13}	0.89	3×10^{-3}
zyg-8(RNAi) (N = 24)		1.2×10^{-13}	0.17	4.6×10^{-3}
ptl-1(RNAi) (N = 13)		1.5×10^{-13}	0.557	3.6×10^{-3}
Untreated at the restrictive temperature (N = 11)	0 -> 0.5 Hz	7.4×10^{-14}	0.190	0.0126
zyg-8(or484ts) at the restrictive temperature (N = 12)		1.1×10^{-13}	9.2×10^{-4}	1.3×10^{-2}
Untreated (N = 9)	0.02 -> 0.5 Hz	7.3×10^{-14}	0.171	1.1×10^{-2}
zyg-8 overexpression (N = 11)		4.8×10^{-14}	0.121	2.1×10^{-2}
RNAi control (N = 17)	0.02 -> 0.3 Hz	3.6×10^{-14}	0.133	1.8×10^{-2}
spd2(RNAi) (N = 19)		4.8×10^{-14}	0.187	1.7×10^{-2}

Table S3: Mechanical parameters measured during anaphase, including the diffusion coefficient (D) and two corner frequencies (f_c and f_0), and obtained by fitting the experimental power spectra of spindle positional micromovements along the transverse axis within the specified frequency interval using a second-order model (Method M13).

4- Supplemental files

The three *Cytosim* simulation files can be downloaded using the following link.
https://sdrive.cnrs.fr/s/MMGgK4P8WRLddTa

5- References

Daniels, B.R., B.C. Masi, and D. Wirtz. 2006. Probing single-cell micromechanics in vivo: the microrheology of C. elegans developing embryos. *Biophysical journal*. 90:4712-4719.

Decker, M., S. Jaensch, A. Pozniakovsky, A. Zinke, Kevin F. O'Connell, W. Zachariae, E. Myers, and Anthony A. Hyman. 2011. Limiting Amounts of Centrosome Material Set Centrosome Size in C. elegans Embryos. *Current Biology*. 21:1259-1267.

Dogterom, M., and B. Yurke. 1997. Measurement of the force-velocity relation for growing microtubules. *Science*. 278:856-860.

Encalada, S.E., P.R. Martin, J.B. Phillips, R. Lyczak, D.R. Hamill, K.A. Swan, and B. Bowerman. 2000. DNA Replication Defects Delay Cell Division and Disrupt Cell Polarity in Early Caenorhabditis elegans Embryos. *Developmental Biology*. 228:225-238.

Grill, S.W., J. Howard, E. Schaffer, E.H.K. Stelzer, and A.A. Hyman. 2003. The distribution of active force generators controls mitotic spindle position. *Science*. 301:518.

McNally, K., A. Audhya, K. Oegema, and F.J. McNally. 2006. Katanin controls mitotic and meiotic spindle length. *The Journal of cell biology*. 175:881-891.

Oegema, K., A. Desai, S. Rybina, M. Kirkham, and A.A. Hyman. 2001. Functional analysis of kinetochore assembly in Caenorhabditis elegans. *The Journal of Cell Biology*. 153:1209-1226.

Praitis, V., E. Casey, D. Collar, and J. Austin. 2001. Creation of Low-Copy Integrated Transgenic Lines in Caenorhabditis elegans. *Genetics*. 157:1217-1226.

Srayko, M., A. Kaya, J. Stamford, and A.A. Hyman. 2005. Identification and Characterization of Factors Required for Microtubule Growth and Nucleation in the Early C. elegans Embryo. *Developmental Cell*. 9:223-236.

Sugioka, K., L.-E. Fielmich, K. Mizumoto, B. Bowerman, S. van den Heuvel, A. Kimura, and H. Sawa. 2018. Tumor suppressor APC is an attenuator of spindle-pulling forces during C. elegans asymmetric cell division. *Proceedings of the National Academy of Sciences*:201712052.

Tarailo, M., S. Tarailo, and A.M. Rose. 2007. Synthetic lethal interactions identify phenotypic “interologs” of the spindle assembly checkpoint components. *Genetics*. 177:2525-2530.

Woodruff, J.B., O. Wueseke, V. Viscardi, J. Mahamid, S.D. Ochoa, J. Bunkenborg, P.O. Widlund, A. Pozniakovsky, E. Zanin, S. Bahmanyar, A. Zinke, S.H. Hong, M. Decker, W. Baumeister, J.S. Andersen, K. Oegema, and A.A. Hyman. 2015. Regulated assembly of a supramolecular centrosome scaffold in vitro. *Science*. 348:808-812.